J. Fluid Mech. (2020), vol. 899, A15.
doi:10.1017/jfm.2020.465

Thermodynamically consistent phase-field modelling of contact angle hysteresis

Pengtao Yue [1]†

[1]Department of Mathematics, Virginia Tech, Blacksburg, VA 24061, USA

(Received xx; revised xx; accepted xx)

In the phase-field description of moving contact line problems, the two-phase system can be described by free energies, and the constitutive relations can be derived based on the assumption of energy dissipation. In this work, we propose a novel boundary condition for contact-angle hysteresis by exploring wall energy relaxation, which allows the system to be in non-equilibrium at the contact line. Our method captures pinning, advancing, and receding automatically without the explicit knowledge of contact-line velocity and contact angle. The microscopic dynamic contact angle is computed as part of the solution instead of being imposed. Furthermore, the formulation satisfies a dissipative energy law, where the dissipation terms all have their physical origin. Based on the energy law, we develop an implicit finite-element method that is second order in time. The numerical scheme is proven to be unconditionally energy-stable for matched density and zero contact angle hysteresis, and is numerically verified to be energy-dissipative for a broader range of parameters. We benchmark our method by computing pinned drops and moving interfaces in the plane Poiseuille flow. When the contact line moves, its dynamics agrees with the Cox theory. In the test case of oscillating drops, the contact line transitions smoothly between pinning, advancing, and receding. Our method can be directly applied to three-dimensional problems as demonstrated by the test case of sliding drops on an inclined wall.

1. Introduction

In reality, most solid surfaces are intrinsically rough or chemically heterogeneous. As a consequence, the contact line may get pinned at the topological or chemical defects and results in non-unique values in the static contact angle (a.k.a. the equilibrium contact angle). The maximum and minimum static contact angles are referred to as the advancing (θ_A) and receding (θ_R) angles; their difference $\theta_A - \theta_R$ is known as the contact angle hysteresis (CAH) (Dussan V. 1979; Quéré 2008). There has been a sizable body of literature exploring the underlying physics of CAH (e.g., Extrand 2002; Gao & McCarthy 2006; Whyman *et al.* 2008; Makkonen 2017; Wu & Ma 2017). The readers are referred to Eral *et al.* (2013); Extrand (2016) for recent reviews on this topic. It should be noted that CAH is even observed on inherently smooth and homogeneous surfaces (Rahimi & Ward 2005). Thus CAH is ubiquitous and should be considered in contact line simulations if possible.

Contact angle hysteresis can be computationally reproduced if topological or chemical heterogeneities on the solid wall are sufficiently resolved. For example, the phase-field method has been successfully used to investigate CAH on chemically heterogeneous (Kusumaatmaja & Yeomans 2007; Wylock *et al.* 2012) surfaces and topologically rough (Luo *et al.* 2017) surfaces. There were also many theoretical works aiming to predict

† Email address for correspondence: ptyue@vt.edu

advancing and receding angles based on chemical and topological patterns (Iwamatsu 2006; Xu & Wang 2011, 2013).

We do not intend to explore the microscopic origin of contact angle hysteresis. Instead, we focus on numerical simulations at length scales much greater than the characteristic scales of the topological or chemical heterogeneities. At this macroscopic level, the solid surface can be considered smooth and θ_A and θ_R can be treated as measurable constants associated with the given system. The contact line is pinned if the contact angle is within the hysteresis window $[\theta_R, \theta_A]$ and moves if otherwise. This is much more computationally affordable than treating the surface as topologically or chemically patterned. The most popular approach for CAH was developed by Spelt (2005) for a level-set method. In this approach, an intermediate contact angle is obtained such that the contact line is pinned. If this angle is within the hysteresis window, the solution is accepted; otherwise, the solution is abandoned and the contact line is moved with prescribed contact angles. This approach was widely adopted and later extended to the phase-field (Ding & Spelt 2008; Huang *et al.* 2014), volume-of-fluid (Dupont & Legendre 2010; Maglio & Legendre 2014; Linder *et al.* 2015), and lattice Boltzmann methods (Wang *et al.* 2013; Ba *et al.* 2013; Liu *et al.* 2015). However, this approach requires ghost cells outside the boundary to impose the contact angle condition or pin the contact line, which can be challenging on curved boundaries and unstructured meshes. Furthermore, to capture slip lengths much smaller than the mesh size, a macroscale model has to be used to find the dynamic contact angle on the boundary. This requires an accurate evaluation of the contact line velocity, which can be tricky to compute due to complications from the wedge flow (Linder *et al.* 2015; Afkhami *et al.* 2018). Recently, Shin *et al.* (2018) introduced an extended interface approach to model CAH in a front tracking method, where the generalized Navier boundary condition (GNBC) (Qian *et al.* 2003) was adopted for the moving contact line. This method, however, still requires ghost cells to impose CAH condition and a hydrodynamic model to impose the dynamic contact angle.

The phase-field method, a.k.a. the diffuse-interface method, has turned into a favorable numerical tool for moving contact line problems since the pioneering work of Jacqmin (2000). The built-in Cahn-Hilliard diffusion automatically regularizes the stress singularity at the moving contact line. Another benefit is its energy formulation, which can be used to guide the design of energy-stable numerical schemes, such as convex splitting (Eyre 1998), linear stabilization (Shen & Yang 2010; Shen *et al.* 2015; Yu & Yang 2017), invariant energy quadratization (Yang 2016), and scalar auxiliary variable (Shen *et al.* 2018) methods. In this work, we will develop a boundary condition for CAH based on wall energy relaxation. Our method does not require ghost cells or the evaluation of contact angle or contact line velocity. More importantly, the energy formulation is preserved. It should be noted that, in the literature, the first phase-field model for CAH was proposed by Vedantam & Panchagnula (2007): an Allen-Cahn equation on the solid surface was used to model liquid spreading. But no fluid flow was considered and the whole setup was purely phenomenological. It is thus totally different from the current work.

The rest of this paper is organized as follows. We first introduce the governing equations for contact line problems without CAH in Section 2. We then develop the CAH model in Section 3, where we also prove the dissipative energy law. The weak form together with numerical discretization is provided in Section 4. Numerical results including benchmarks are given in Section 5, where we also come up with a computational strategy for CAH. For readers' convenience, the following technical topics are included in the appendices: the derivation of wall energy is given in Appendix A; constitutive relations, including GNBC, are derived based on the second law of thermodynamics in Appendix B; compressibility caused by Cahn-Hilliard diffusion is discussed in Appendix C.

2. Phase-field method for moving contact lines

We consider an incompressible two-phase system of Newtonian fluids in domain Ω and in contact with a solid wall $\partial\Omega_w$ which is a subset of the domain boundary $\partial\Omega$. We introduce a phase-field variable ϕ, which changes from +1 in fluid 1 to -1 in fluid 2. The total free energy, including the kinetic energy, can be written as

$$\mathcal{F} = \int_\Omega \left(f_m(\phi, \nabla\phi) + \frac{1}{2}\rho|\boldsymbol{u}|^2 \right) d\boldsymbol{x} + \int_{\partial\Omega_w} f_w(\phi) ds, \tag{2.1}$$

where

$$f_m(\phi, \nabla\phi) = \lambda \left(\frac{1}{2}|\nabla\phi|^2 + f_0(\phi) \right) \tag{2.2}$$

is the mixing energy per unit volume (Cahn & Hilliard 1958),

$$f_0(\phi) = \frac{(\phi^2 - 1)^2}{4\epsilon^2} \tag{2.3}$$

is the double-well potential, and

$$f_w(\phi) = -\sigma \cos\theta_S \frac{\phi(3 - \phi^2)}{4} \tag{2.4}$$

is the surface energy per unit area on the wall (Cahn 1977; Jacqmin 2000). Here ρ is the fluid density, $\boldsymbol{u}$ is the fluid velocity, λ is the mixing energy density, ϵ is the capillary width, σ is the surface tension, and θ_S is the static contact angle (a.k.a. equilibrium contact angle) defined in fluid 1 ($\phi = 1$). For a 1D diffuse interface in equilibrium, we have (Yue *et al.* 2004)

$$\sigma = \frac{2\sqrt{2}}{3}\frac{\lambda}{\epsilon} \tag{2.5}$$

and

$$\phi(x) = \tanh\left(\frac{x}{\sqrt{2}\epsilon} \right) \tag{2.6}$$

where we have assumed that the diffuse interface is centered at $x = 0$. The derivation of f_w can be found in Appendix A.

The free energy (2.1) leads to to following coupled system of Navier-Stokes and Cahn-Hilliard equations:

$$\rho \left(\frac{\partial \boldsymbol{u}}{\partial t} + \boldsymbol{u} \cdot \nabla \boldsymbol{u} \right) + \boldsymbol{J} \cdot \nabla \boldsymbol{u} = -\nabla p + \nabla \cdot \boldsymbol{\tau} + G\nabla\phi + \rho \boldsymbol{g}, \tag{2.7}$$

$$\nabla \cdot \boldsymbol{u} = 0, \tag{2.8}$$

$$\frac{\partial \phi}{\partial t} + \boldsymbol{u} \cdot \nabla\phi = \nabla \cdot (M\nabla G), \tag{2.9}$$

$$G = \lambda(-\Delta\phi + f_0'(\phi)), \tag{2.10}$$

where ρ is the density, $\boldsymbol{u}$ is the volume-averaged velocity, $\boldsymbol{J}$ is a diffusive flux caused by the discrepancy between $\boldsymbol{u}$ and the mass-averaged velocity (Abels *et al.* 2012), $\boldsymbol{\tau} = \mu\left(\nabla\boldsymbol{u} + (\nabla\boldsymbol{u})^T\right)$ is the viscous stress, μ is the viscosity, and G is the chemical potential. It should be noted that the Cahn-Hilliard equation is split into two second order equations (2.9) and (2.10). This is a common treatment in finite element methods (Yue *et al.* 2006; Khatavkar *et al.* 2007*b*), because the C^0 finite elements cannot handle fourth order derivatives directly. These equations are complemented by the following boundary

conditions:

$$\boldsymbol{u} = \boldsymbol{u}_w \quad \text{on } \partial\Omega_w, \tag{2.11}$$

$$\boldsymbol{n}\cdot\nabla G = 0 \quad \text{on } \partial\Omega, \tag{2.12}$$

$$\frac{\partial\phi}{\partial t} + \boldsymbol{u}\cdot\nabla\phi = -\Gamma L(\phi,\nabla\phi) \quad \text{on } \partial\Omega_w, \tag{2.13}$$

$$\boldsymbol{n}\cdot\nabla\phi = 0 \quad \text{on } \partial\Omega\backslash\partial\Omega_w, \tag{2.14}$$

where $\boldsymbol{u}_w$ is the wall velocity, Γ is a positive phenomenological parameter that controls the rate of wall energy relaxation, and

$$L(\phi,\nabla\phi) = \lambda\boldsymbol{n}\cdot\nabla\phi + f_w'(\phi) \tag{2.15}$$

is the wall potential. Equations (2.11–2.13) correspond to the no-slip, zero diffusive flux, and wall energy relaxation conditions, respectively. Equation (2.14) corresponds to a homogeneous natural boundary condition, which does not require any special attention in the finite element methods. The interested readers are referred to Appendices B and C for the derivation of these equations. On $\partial\Omega\backslash\partial\Omega_w$, i.e., boundaries other than solid walls, additional velocity or stress conditions are required depending on the particular problem.

In our phase-field formulation, ϕ is related to volume fraction and the mixture properties are computed by

$$\rho(\phi) = \frac{1+\phi}{2}\rho_1 + \frac{1-\phi}{2}\rho_2, \quad \mu(\phi) = \frac{1+\phi}{2}\mu_1 + \frac{1-\phi}{2}\mu_2, \tag{2.16}$$

where subscripts $_1$ and $_2$ denote the properties of the pure fluids 1 and 2, respectively. Then, according to (B 13) and (C 4), the diffusive mass flux can be written as

$$\boldsymbol{J} = -\frac{\rho_1-\rho_2}{2}M\nabla G. \tag{2.17}$$

The wall energy relaxation (2.13), together with the no-slip condition (2.11), is a special case of GNBC. It works together with interface mobility to generated the desired slip length (Yue & Feng 2011). According to Carlson *et al.* (2011), the wall energy relaxation accounts for the dissipation due to the re-organization of molecules at the contact line.

For a planar interface, θ_S is recovered exactly if $L = 0$, i.e., when the system is in equilibrium at the contact line. Equation (2.13) allows the contact line to deviate from equilibrium, i.e., $L \neq 0$ when contact line moves. This causes the actual microscopic contact angle measured at the wall (see Fig. 5b), termed the dynamic contact angle θ_D, to deviate from θ_S. This deviation has been confirmed by various molecular-dynamics studies (Ren & E 2007; Fernández-Toledano *et al.* 2019). Alternatively, if we assume the microscopic angle to stay at its equilibrium value θ_S, then θ_D in the phase-field model can be viewed as the interface angle at a distance of $\mathcal{O}(l_D)$ to the contact line, where $l_D = \sqrt{M\mu}$ is the diffusion length and μ is an effective viscosity (Yue *et al.* 2010; Yue & Feng 2011). Numerically, this θ_D plays a role similar to the intermediate angle in the macroscale approach of Spelt (2005) and the numerical angle in the mesh-independent volume-of-fluid method of Afkhami *et al.* (2009). The major difference is that our θ_D is automatically obtained from the phase-field simulations instead of being manually imposed based on external models such as the hydrodynamic model developed by Voinov (1976) and Cox (1986).

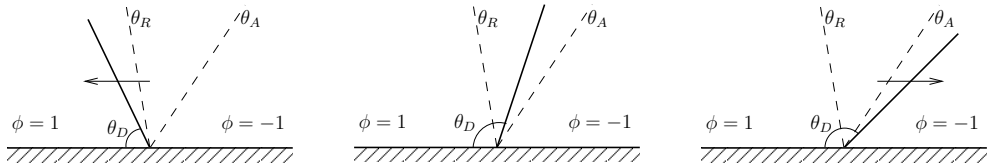

(a) Receding, $\theta_D < \theta_R$ (b) Pinned, $\theta_R \leqslant \theta_D \leqslant \theta_A$ (c) Advancing, $\theta_D > \theta_A$

Figure 1: Different states of a contact line with CAH. We define the advancing and receding states with respect to the $\phi = 1$ fluid.

3. Contact angle hysteresis

3.1. *Boundary condition for contact angle hysteresis*

On the solid wall, the motion of the contact line is directly related to the variation of ϕ: Contact line advances if $\frac{D\phi}{Dt} > 0$ (i.e., the region previously occupied by $\phi = -1$ is now occupied by $\phi = 1$), recedes if $\frac{D\phi}{Dt} < 0$, and is pinned if $\frac{D\phi}{Dt} = 0$. Here $\frac{D}{Dt} = \frac{\partial}{\partial t} + \boldsymbol{u} \cdot \nabla$ denotes the material derivative, and in particular $\frac{D}{Dt} = \frac{\partial}{\partial t}$ on fixed walls. Meanwhile, θ_D is embedded in the $\boldsymbol{n} \cdot \nabla\phi$ term of the wall potential L. We have $L < 0$ if $\theta_D > \theta_S$, $L > 0$ if $\theta_D < \theta_S$, and $L = 0$ if $\theta_D = \theta_S$. Interested readers are referred to Appendix A for more details. Thus we recover the criterion for contact line motion: contact line advances (or recedes) if $\theta_D > \theta_S$ (or $\theta_D < \theta_S$) and is pinned if $\theta_D = \theta_S$.

When CAH exists, the static contact angle has non-unique values, the maximum of which is the advancing contact angle θ_A and the minimum of which is the receding contact angle θ_R. The contact line advances if $\theta_D > \theta_A$, recedes if $\theta_D < \theta_R$, and is pinned if $\theta_R \leqslant \theta_D \leqslant \theta_A$, as illustrated in Fig. 1.

For convenience, we rewrite the wall energy as

$$f_w(\phi; \theta) = -\sigma \cos\theta \frac{\phi(3 - \phi^2)}{4}, \tag{3.1}$$

where the contact angle θ is included as a parameter. For the physically relevant range $\phi \in [-1, 1]$,

$$f_w'(\phi; \theta) = -\frac{3}{4}\sigma \cos\theta (1 - \phi^2) \tag{3.2}$$

is an increasing function in θ, where $'$ denotes the derivative in the first argument. It follows that $L(\phi, \nabla\phi; \theta) = \lambda \boldsymbol{n} \cdot \nabla\phi + f_w'(\phi; \theta)$ is also an increasing function in θ. For brevity, we denote $L(\phi, \nabla\phi; \theta_A)$ by L_A and $L(\phi, \nabla\phi; \theta_R)$ by L_R.

For a contact line with dynamic angle θ_D, the contact line would be in equilibrium if θ_D were also the static contact angle; it follows that $L(\phi, \nabla\phi; \theta_D) = 0$, i.e., $\lambda \boldsymbol{n} \cdot \nabla\phi = -f_w'(\phi; \theta_D)$. This is exactly (A 7) in Appendix A. Then the relations between θ_D, θ_A, and θ_R can be mapped to the relations between the wall potentials associated with these angles:

- advancing contact line ($\frac{D\phi}{Dt} > 0$) $\Leftrightarrow \theta_D > \theta_A > \theta_R \Leftrightarrow 0 > L_A > L_R$;
- receding contact line ($\frac{D\phi}{Dt} < 0$) $\Leftrightarrow \theta_A > \theta_R > \theta_D \Leftrightarrow L_A > L_R > 0$;
- pinned contact line ($\frac{D\phi}{Dt} = 0$) $\Leftrightarrow \theta_A \geqslant \theta_D \geqslant \theta_R \Leftrightarrow L_A \geqslant 0 \geqslant L_R$.

Apparently, the state (advancing, receding, or pinned) of the contact line can be determined by comparing the values of L_A and L_R. This motivates the following equation in place of (2.13) on $\partial\Omega_w$:

$$\frac{\partial\phi}{\partial t} + \boldsymbol{u} \cdot \nabla\phi = -\Gamma \tilde{L}, \tag{3.3}$$

where

$$\tilde{L} = \mathrm{minmod}(L_A, L_R). \tag{3.4}$$

Here we have used the minmod function

$$\mathrm{minmod}(a,b) = \begin{cases} \mathrm{sign}(a)\min(|a|,|b|) & \text{if } ab > 0 \\ 0 & \text{otherwise} \end{cases},$$

which returns the argument with the smaller magnitude if both arguments have the same sign and zero if otherwise. This equation pins the contact line if $\theta_D \in [\theta_R, \theta_A]$. If the contact line moves, it automatically picks the correct static contact angle: θ_A if contact line advances and θ_R if contact line recedes. It should be noted that, at the leading order, (3.3) is consistent with Eq. (6) in Prabhala & Panchagnula (2013) for quasi-static computations of drop shapes on hysteric surfaces.

This boundary condition is very easy to implement numerically. In each cell face on the solid wall, we compute the two copies of wall potentials, namely, $L(\phi, \nabla\phi; \theta_A)$ and $L(\phi, \nabla\phi; \theta_R)$. Then we compare the cell average of this two potentials, and decide which one (including 0) we need to take into (3.3). There is no need to extract θ_D or contact line velocity.

3.2. *Energy law for contact angle hysteresis*

In thermodynamics, hysteresis cannot be described by a path-independent state function. Therefore we cannot find a single-valued wall energy to describe the contact line motion with CAH. However, that does not prevent the system from satisfying the a dissipative energy law.

THEOREM 1. *The equation system* (2.7)–(2.10)*, together with the boundary conditions* (2.11)*,* (2.12)*,* (2.14)*, and* (3.3)*, satisfies the following energy law*

$$\frac{d}{dt}\left\{\int_\Omega \left(\frac{1}{2}\rho|\boldsymbol{u}|^2 + f_m\right) d\boldsymbol{x} + \int_{\partial\Omega_w} f_w(\phi;\theta_A) ds\right\} = \mathcal{W} - \mathcal{D} - \mathcal{D}_{cah}, \tag{3.5}$$

where

$$\mathcal{W} = \oint_{\partial\Omega} \boldsymbol{n}\cdot\boldsymbol{T}\cdot\boldsymbol{u} ds + \int_\Omega \rho\boldsymbol{g}\cdot\boldsymbol{u} d\boldsymbol{x}$$

is the power of the reversible work done by the boundary and body force,

$$\mathcal{D} = \int_\Omega \boldsymbol{\tau} : \nabla\boldsymbol{u} d\boldsymbol{x} + \int_\Omega M|\nabla G|^2 d\boldsymbol{x} + \int_{\partial\Omega_w} \Gamma\tilde{L}^2 ds \geqslant 0$$

is the dissipation rate as seen in the standard contact line problem, and

$$\mathcal{D}_{cah} = \int_{\partial\Omega_w} [f_w'(\phi;\theta_R) - f_w'(\phi;\theta_A)]\min(\frac{D\phi}{Dt}, 0) ds \geqslant 0$$

is the dissipation rate due to CAH. Here $\boldsymbol{T} = -p\boldsymbol{I} + \boldsymbol{\tau} + \boldsymbol{\tau}_\phi$ *is the total stress and* $\boldsymbol{\tau}_\phi$ *is given by* (B 7)*. The term in the curly braces is the "free energy" including the kinetic energy, the mixing energy, and the wall energy based on the advancing contact angle.*

Proof.

To save space, we will focus on the proof related to CAH and only provide a sketch for the rest.

From (2.9), (2.16), and (2.17), we recover

$$\frac{D\rho}{Dt} = \frac{\rho_1 - \rho_2}{2}\frac{D\phi}{Dt} = \frac{\rho_1 - \rho_2}{2}\nabla\cdot(M\nabla G) = -\nabla\cdot\boldsymbol{J}. \tag{3.6}$$

By taking the inner product of (2.7) and $\boldsymbol{u}$, taking the inner product of (3.6) and $\frac{|\boldsymbol{u}|^2}{2}$, and summing them up, we obtain

$$\frac{d}{dt}\int_{\Omega}\frac{1}{2}\rho|\boldsymbol{u}|^2 d\boldsymbol{x} = \oint_{\partial\Omega}\boldsymbol{n}\cdot\boldsymbol{T}\cdot\boldsymbol{u}ds + \int_{\Omega}\rho\boldsymbol{g}\cdot\boldsymbol{u}d\boldsymbol{x} - \int_{\Omega}\boldsymbol{T}:\nabla\boldsymbol{u}. \tag{3.7}$$

Here we have used the incompressibility condition (2.8) and replaced $G\nabla\phi$ with $\nabla\cdot\boldsymbol{\tau}_{\phi}$ based on the identity (B 19). The derivation of this equation is essentially the same as (C 6). The only difference is that we now include a body force and replace $\tilde{\boldsymbol{T}}$ with $\boldsymbol{T}$.

By taking the inner product of (2.9) and G, taking the inner product of (2.10) with $-\frac{D\phi}{Dt}$, and summing them up, we get

$$\frac{d}{dt}\int_{\Omega}f_m d\boldsymbol{x} = \int_{\partial\Omega_w}\lambda\boldsymbol{n}\cdot\nabla\phi\frac{D\phi}{Dt}ds + \int_{\Omega}\boldsymbol{\tau}_{\phi}:\nabla\boldsymbol{u}d\boldsymbol{x} - \int_{\Omega}M|\nabla\phi|^2 d\boldsymbol{x}, \tag{3.8}$$

where we have considered (2.14). The proof of this equation is essentially the reverse of (B 5).

The $\tilde{L}$ term in (3.3) takes different values depending on the state of the contact line. If the contact line advances, we have $\frac{D\phi}{Dt} = \frac{\partial\phi}{\partial t} + \boldsymbol{u}_w\cdot\nabla\phi > 0$ and $\tilde{L} = L_A = \lambda\boldsymbol{n}\cdot\nabla\phi + f_w'(\phi;\theta_A)$ on $\partial\Omega_w$; if the contact line recedes, we have $\frac{D\phi}{Dt} < 0$ and $\tilde{L} = L_R = \lambda\boldsymbol{n}\cdot\nabla\phi + f_w'(\phi;\theta_R)$; if the contact line is pinned, we have $\frac{D\phi}{Dt} = 0$ and $\tilde{L} = 0$. This leads to the following identity

$$\begin{aligned}\tilde{L}\frac{D\phi}{Dt} &= \lambda\boldsymbol{n}\cdot\nabla\phi\frac{D\phi}{Dt} + f_w'(\phi;\theta_A)\max(\frac{D\phi}{Dt},0) + f_w'(\phi;\theta_R)\min(\frac{D\phi}{Dt},0)\\ &= [\lambda\boldsymbol{n}\cdot\nabla\phi + f_w'(\phi;\theta_A)]\frac{D\phi}{Dt} + [f_w'(\phi;\theta_R) - f_w'(\phi;\theta_A)]\min(\frac{D\phi}{Dt},0).\end{aligned} \tag{3.9}$$

By taking the inner product of (3.3) and $-\frac{1}{\Gamma}\frac{D\phi}{Dt}$ on $\partial\Omega_w$, and considering (3.9), we obtain

$$\begin{aligned}&\int_{\partial\Omega_w} -\frac{1}{\Gamma}\left(\frac{D\phi}{Dt}\right)^2 ds\\ &= \int_{\partial\Omega_w}\left\{[\lambda\boldsymbol{n}\cdot\nabla\phi + f_w'(\phi;\theta_A)]\frac{D\phi}{Dt} + [f_w'(\phi;\theta_R) - f_w'(\phi;\theta_A)]\min(\frac{D\phi}{Dt},0)\right\}ds\\ &= \int_{\partial\Omega_w}\lambda\boldsymbol{n}\cdot\nabla\phi\frac{D\phi}{Dt}ds + \frac{d}{dt}\int_{\partial\Omega_w}f_w(\phi;\theta_A)ds + \int_{\partial\Omega_w}[f_w'(\phi;\theta_R) - f_w'(\phi;\theta_A)]\min(\frac{D\phi}{Dt},0)ds.\end{aligned} \tag{3.10}$$

Equation (3.5) can be easily obtained by combining (3.7), (3.8), and (3.10).

The positivity of $\mathcal{D}$ is easily seen. Since $\theta_A > \theta_R$, we have $f_w'(\phi;\theta_A) > f_w'(\phi;\theta_R)$ based on (3.2). Thus both $f_w'(\phi;\theta_R) - f_w'(\phi;\theta_A)$ and $\min(\frac{D\phi}{Dt},0)$ are non-positive, and $\mathcal{D} \geqslant 0$ follows.

□

Remark 1. *This theorem neither assumes the fluid domain Ω to be fixed, nor does it require $\boldsymbol{n}\cdot\boldsymbol{u} = 0$ on the boundary. It should be noted that* (3.5) *can also be cast into*

$$\frac{d}{dt}\left\{\int_{\Omega}\left(\frac{1}{2}\rho|\boldsymbol{u}|^2 + f_m\right)d\boldsymbol{x} + \int_{\partial\Omega_w}f_w(\phi;\theta_R)ds\right\} = \mathcal{W} - \mathcal{D} - \tilde{\mathcal{D}}_{cah} \tag{3.11}$$

with

$$\tilde{\mathcal{D}}_{cah} = \int_{\partial\Omega_w}[f_w'(\phi;\theta_A) - f_w'(\phi;\theta_R)]\max(\frac{D\phi}{Dt},0)ds \geqslant 0$$

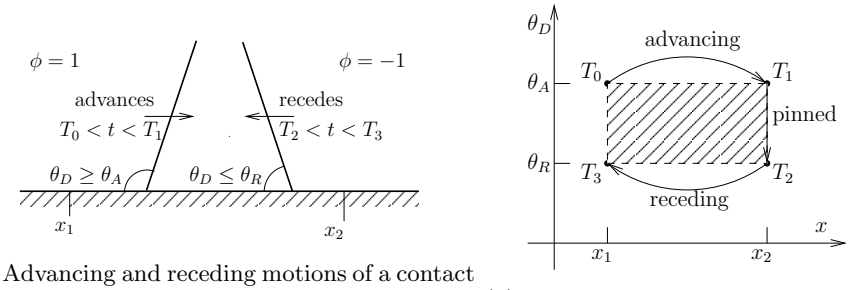

(a) Advancing and receding motions of a contact line.

(b) Hysteresis loop in the x–θ_D plane.

Figure 2: Dissipations due to contact line motion. The contact line advances from x_1 to x_2 and then recedes back to x_1.

It is obvious that $\mathcal{D}_{cah} = 0$ if the contact line never recedes and $\tilde{\mathcal{D}}_{cah} = 0$ if the contact line never advances. The dissipation of CAH takes action only when a region on the solid surface is swept by both an advancing contact line and a receding contact line.

It should be noted that the "free energy" in (3.5) *can not be understood in the traditional sense. Not all this "free energy" can be used to do work and the portion that can do work is path-dependent. For example, if we use θ_A to define the wall energy, then all the "free energy" can do work if the contact line advances; but if the contact line recedes, only part of the "free energy" can do work and the missing part is $\mathcal{D}_{cah}$. Similarly, if we use θ_R, then only part of the "free energy" can do work when the contact line advances and the missing part is $\tilde{\mathcal{D}}_{cah}$.*

In the following, we provide a physical explanation to the dissipation terms that occur on the solid wall. We consider a contact line problem in 2D with a stationary solid wall (such that $\frac{D\phi}{Dt} = \frac{\partial \phi}{\partial t}$) for simplicity. Suppose a contact line advances over a region $A = [x_1, x_2]$ with length $a = x_2 - x_1$ on the solid wall at $t \in [T_0, T_3]$, as illustrated in Fig. 2. At $t = T_0$, the contact line starts from x_1 with $\theta_D = \theta_A$. Then the contact line advances with $\theta_D \geqslant \theta_A$ and arrives at x_1 at $t = T_1$. During $[T_1, T_2]$ the contact line is pinned at x_2 and adjusts its microscopic contact angle from θ_A to θ_R. Then the contact line recedes with $\theta_D \leqslant \theta_R$ and returns to its original position x_1 at $t = T_3$.

In the phase-field context, we have $\phi = -1$ at $t = T_0$, $\phi = 1$ at $t \in [T_1, T_2]$, and $\phi = -1$ again at $t = T_3$ in A. Correspondingly, $\frac{\partial \phi}{\partial t} \geqslant 0$ at $t \in [T_0, T_1]$, $= 0$ at $t \in [T_1, T_2]$, and $\frac{\partial \phi}{\partial t} \leqslant 0$ at $t \in [T_2, T_3]$. Then the energy dissipated due to CAH is

$$\begin{aligned}
\int_{T_0}^{T_3} \mathcal{D}_{cah} dt &= \int_{T_0}^{T_3} \int_A [f_w'(\phi;\theta_R) - f_w'(\phi;\theta_A)] \min(\frac{\partial \phi}{\partial t}, 0) ds dt \\
&= \int_A \int_{T_2}^{T_3} [f_w'(\phi;\theta_R) - f_w'(\phi;\theta_A)] \frac{\partial \phi}{\partial t} dt ds \\
&= \int_A \int_{\phi=1}^{\phi=-1} [f_w'(\phi;\theta_R) - f_w'(\phi;\theta_A)] d\phi ds \\
&= \int_A \left[f_w(\phi;\theta_R)|_{\phi=1}^{\phi=-1} - f_w(\phi;\theta_A)|_{\phi=1}^{\phi=-1} \right] ds = \sigma(\cos\theta_R - \cos\theta_A) a, \quad (3.12)
\end{aligned}$$

which is non-negative because $\theta_R \leqslant \theta_A$. This corresponds to the region enclosed by $x = x_1$, $x = x_2$, $\theta_D = \theta_A$, and $\theta_D = \theta_R$, which is shaded in Fig. 2(b). The same amount of dissipation can also be be obtained using $\mathcal{D}_{cah}^*$.

Meanwhile, during $[T_0, T_1]$, the dissipation due to the deviation of θ_D from θ_A is

$$\begin{aligned}\int_{T_0}^{T_1}\int_A \Gamma\tilde{L}^2 ds dt &= \int_{T_0}^{T_1}\int_A \Gamma L_A^2 ds dt = \int_A\int_{T_0}^{T_1} -L_A\frac{\partial\phi}{\partial t}dt ds\\ &= \int_A\int_{T_0}^{T_1}(f_w'(\phi;\theta_D) - f_w'(\phi;\theta_A))\frac{\partial\phi}{\partial t}dt ds\\ &= \int_A\left[f_w(\phi;\theta_D)|_{\phi=-1}^{\phi=1} - f_w(\phi;\theta_A)|_{\phi=-1}^{\phi=1}\right]ds\\ &= \sigma(\cos\theta_A - \cos\theta_D)a, \end{aligned} \tag{3.13}$$

where we have used the relation $\lambda\boldsymbol{n}\cdot\nabla\phi = -f_w'(\phi;\theta_D)$ (see (A 7)) in the third equality. This corresponds to the region enclosed by the advancing branch of θ_D and $\theta_D = \theta_A$ in Fig. 2(b). It should be noted a tangential force of $\sigma\cos\theta_D$ has to be exerted at the contact line in order to move the interface with a contact angle θ_D while the wettability supplies a force of $\sigma\cos\theta_A$. The difference between these two forces, which has been referred to as the uncompensated (Qian *et al.* 2003) or unbalanced (Ren & E 2007) Young's stress in the literature, is responsible for the additional dissipation in (3.13). Similarly, we can get the dissipation due to the deviation of θ_D from θ_R during $[T_2, T_3]$:

$$\int_{T_2}^{T_3}\int_A \Gamma\tilde{L}^2 ds dt = \sigma(\cos\theta_D - \cos\theta_R)a, \tag{3.14}$$

which corresponds to the region enclosed by $\theta_D = \theta_R$ and the receding branch of θ_D. A complete hysteresis loop is formed if the contact line stays pinned at x_1 at $t \geqslant T_3$ and θ_D changes from θ_R to θ_A. This pinned state does not cause any dissipation on the solid wall (of course, viscous dissipation in the bulk may be incurred to deform the interface away from the contact line). The argument here can be easily extended to 3D flows, where A is a 2D region on the wall boundary and a is the area of A.

4. Numerical discretization

4.1. *Weak form and discrete energy law*

The weak form of the governing equations (2.7)–(2.10) and (3.3) can be expressed as

$$\begin{aligned}\left(\rho\frac{D\boldsymbol{u}}{Dt} + \boldsymbol{J}\cdot\nabla\boldsymbol{u}, \hat{\boldsymbol{u}}\right) &= (\boldsymbol{n}\cdot(-p\boldsymbol{I}+\boldsymbol{\tau}), \hat{\boldsymbol{u}})_{\partial\Omega} - (-p\boldsymbol{I}+\boldsymbol{\tau}, \nabla\hat{\boldsymbol{u}})\\ &\quad + (G\nabla\phi + \rho\boldsymbol{g}, \hat{\boldsymbol{u}}), \end{aligned} \tag{4.1}$$

$$-(\nabla\cdot\boldsymbol{u}, \hat{p}) = 0, \tag{4.2}$$

$$\left(\frac{D\phi}{Dt}, \hat{\phi}\right) = \left(M\nabla G, \nabla\hat{\phi}\right), \tag{4.3}$$

$$\left(G, \hat{G}\right) - \frac{1}{\Gamma}\left(\frac{D\phi}{Dt}, \hat{G}\right)_{\partial\Omega_w} = (\lambda\nabla\phi, \nabla\hat{G}) + (\lambda f_0'(\phi), \hat{G}) + \left(A, \hat{G}\right)_{\partial\Omega_w}, \tag{4.4}$$

where $(\cdot,\cdot)$ denotes the L_2 inner product in the domain Ω, $(\cdot,\cdot)_{\partial\Omega}$ and $(\cdot,\cdot)_{\partial\Omega_w}$ denote the inner product on $\partial\Omega$ and $\partial\Omega_w$. We seek solutions $\boldsymbol{u}\in H^1(\Omega)^d$, $p\in L^2(\Omega)$, $\phi\in H^1(\Omega)$, and $G\in H^1(\Omega)$ satisfying the equations above, where d is the dimension of the problem. The variables with $\hat{}$ are the corresponding test functions. The special form of (4.4) is motivated by the proof of Theorem 1. The $\lambda\boldsymbol{n}\cdot\nabla\phi$ term in $\tilde{L}$ is cancelled out on $\partial\Omega_w$

unless the contact line is pinned. The term A comes from CAH and can be expressed as:

$$A = \begin{cases} f_w'(\phi;\theta_A) = -\frac{3}{4}\sigma\cos\theta_A(1-\phi^2) & \text{if } 0 \geqslant L_A \geqslant L_R \text{ (contact line advances)} \\ f_w'(\phi;\theta_R) = -\frac{3}{4}\sigma\cos\theta_R(1-\phi^2) & \text{if } L_A \geqslant L_R > 0 \text{ (contact line recedes)} \\ -\lambda\boldsymbol{n}\cdot\nabla\phi & \text{otherwise} \end{cases}. \tag{4.5}$$

If $\nabla\cdot\boldsymbol{u} = 0$ is satisfied in the strong sense, then the energy law (3.5) is recovered if we take $\hat{\boldsymbol{u}} = \boldsymbol{u}$, $\hat{\phi} = G$, and $\hat{G} = \frac{D\phi}{Dt}$. To obtain similar energy law under the weak incompressibility condition (4.2), special cares must be taken on the momentum equation, e.g., the skew-symmetric form for flows with constant density and the method of Guermond & Quartapelle (2000) for flows with variable density.

There have been energy-stable numerical schemes for moving contact line problems with variable densities (e.g., Gao & Wang 2014; Yu & Yang 2017; Metzger 2019). But they are all first-order in time and the time step has to be very small for reasonable temporal accuracy. In this work, we adopt a second-order time discretization based on the Crank-Nicolson method and a skew-symmetric form for the convection term in the momentum equation. In the semi-discrete form, we seek $\boldsymbol{u}^{n+1}$, $p^{n+\frac{1}{2}}$, ϕ^{n+1}, and $G^{n+\frac{1}{2}}$ satisfying

$$\begin{aligned}\left(\rho^{n+\frac{1}{2}}\left(\frac{\boldsymbol{u}^{n+1}-\boldsymbol{u}^n}{\Delta t} + \bar{\boldsymbol{u}}^{n+\frac{1}{2}}\cdot\nabla\boldsymbol{u}^{n+\frac{1}{2}} + \frac{1}{2}(\nabla\cdot\bar{\boldsymbol{u}}^{n+\frac{1}{2}})\boldsymbol{u}^{n+\frac{1}{2}}\right), \hat{\boldsymbol{u}}\right) \\ - \left(\frac{\rho_1-\rho_2}{2}M\nabla G^{n+\frac{1}{2}}\cdot\nabla\boldsymbol{u}^{n+\frac{1}{2}}, \hat{\boldsymbol{u}}\right) \\ = \left(p^{n+\frac{1}{2}}\boldsymbol{I} - \mu^{n+\frac{1}{2}}\boldsymbol{E}(\boldsymbol{u}^{n+\frac{1}{2}}), \nabla\hat{\boldsymbol{u}}\right) + \left(G^{n+\frac{1}{2}}\nabla\phi^{n+\frac{1}{2}}, \hat{\boldsymbol{u}}\right),\end{aligned} \tag{4.6}$$

$$-(\nabla\cdot\boldsymbol{u}^n, \hat{p}) = 0, \tag{4.7}$$

$$\left(\frac{\phi^{n+1}-\phi^n}{\Delta t} + \boldsymbol{u}^{n+\frac{1}{2}}\cdot\nabla\phi^{n+\frac{1}{2}}, \hat{\phi}\right) = (-M\nabla G^{n+\frac{1}{2}}, \nabla\hat{\phi}), \tag{4.8}$$

$$\begin{aligned}(G^{n+\frac{1}{2}}, \hat{G}) - \left(\frac{1}{\Gamma}\left(\frac{\phi^{n+1}-\phi^n}{\Delta t} + \boldsymbol{u}_w\cdot\nabla\phi^{n+\frac{1}{2}}\right), \hat{G}\right)_{\partial\Omega_w} \\ = \left(\lambda\nabla\phi^{n+\frac{1}{2}}, \nabla\hat{G}\right) + \left(\lambda Df_0(\phi^n, \phi^{n+1}), \hat{G}\right) + \sum_{e\in\mathcal{T}(\partial\Omega_w)}\left(A^{n+\frac{1}{2}}, \hat{G}\right)_e,\end{aligned} \tag{4.9}$$

for all admissible test functions $\hat{\boldsymbol{u}}$, $\hat{p}$, $\hat{\phi}$, and $\hat{G}$. Here, $\Delta t = t^{n+1} - t^n$ is the time step, $\boldsymbol{u}^{n+\frac{1}{2}} = \frac{\boldsymbol{u}^{n+1}+\boldsymbol{u}^n}{2}$ and $\phi^{n+\frac{1}{2}} = \frac{\phi^{n+1}+\phi^n}{2}$ are second order approximations at half time level $t^{n+\frac{1}{2}}$, $\bar{\boldsymbol{u}}^{n+\frac{1}{2}} = \frac{3\boldsymbol{u}^n-\boldsymbol{u}^{n-1}}{2}$ ($\bar{\boldsymbol{u}}^{n+\frac{1}{2}} = \boldsymbol{u}^n$ for $n=0$) is an explicit approximation at $t^{n+\frac{1}{2}}$ by extrapolation, $\rho^{n+\frac{1}{2}} = \frac{1+\phi^{n+\frac{1}{2}}}{2}\rho_1 + \frac{1-\phi^{n+\frac{1}{2}}}{2}\rho_2$, $\mu^{n+\frac{1}{2}} = \frac{1+\phi^{n+\frac{1}{2}}}{2}\mu_1 + \frac{1-\phi^{n+\frac{1}{2}}}{2}\mu_2$, $\mathcal{T}(\partial\Omega_w)$ denotes the triangulation of the wall boundary $\partial\Omega_w$, and e denotes an element face (or edge in 2D) on $\partial\Omega_w$. We have also introduced the strain rate tensor $\boldsymbol{E}(\boldsymbol{u}) = \nabla\boldsymbol{u} + (\nabla\boldsymbol{u})^T$ for convenience. The term Df_0, first introduced by Du & Nicolaides (1991) and sometimes referred to as the discrete variational derivative (Gomez & van der Zee 2017), is a second order approximation to $f_0'(\phi^{n+\frac{1}{2}})$ for the purpose of energy stability:

$$Df_0(\phi^n, \phi^{n+1}) = \begin{cases} \frac{f_0(\phi^{n+1})-f_0(\phi^n)}{\phi^{n+1}-\phi^n} & \text{if } \phi^{n+1} \neq \phi^n \\ f_0'(\phi^n) & \text{if } \phi^{n+1} = \phi^n. \end{cases} \tag{4.10}$$

The term $A^{n+\frac{1}{2}}$ takes care of CAH. For the convenience of numerical implementation, we determine the status of contact line by comparing the integral of wall potential. On each element face e on wall boundary, we have

$$A^{n+\frac{1}{2}} = \begin{cases} Df_w(\phi^n, \phi^{n+1}; \theta_A) & \text{if } 0 \geqslant L_A^* \geqslant L_R^* \\ Df_w(\phi^n, \phi^{n+1}; \theta_R) & \text{if } L_A^* \geqslant L_R^* > 0 \\ -\lambda \boldsymbol{n} \cdot \nabla \phi^{n+\frac{1}{2}} & \text{otherwise} \end{cases}, \tag{4.11}$$

where Df_w is the discrete variational derivative of f_w. L_A^* and L_R^* are the integrals of wall potentials on element face and they are defined explicitly for numerical convenience: $L_{A,R}^* = \int_e [\lambda \boldsymbol{n} \cdot \nabla \phi^n + f_w'(\phi^n; \theta_{A,R})]\, ds$.

In most problems, we impose either a zero traction condition $\boldsymbol{n} \cdot \boldsymbol{T} = \boldsymbol{0}$ or a Dirichlet condition for $\boldsymbol{u}$ on the domain boundary, which causes the surface integral term in (4.1) to vanish. Thus, for brevity, the surface integral term is dropped in (4.6).

This scheme does not have unconditional energy stability, but it satisfies the following discrete energy law for matched density.

THEOREM 2. *If $\rho_1 = \rho_2 = \rho$ and $\boldsymbol{u}_w = 0$, then the semi-discrete system* (4.6)–(4.9) *with the non-penetrating essential boundary condition $\boldsymbol{n} \cdot \boldsymbol{u}|_{\partial\Omega} = 0$ satisfies the following discrete energy law*

$$\frac{\mathcal{F}_A^{n+1} - \mathcal{F}_A^n}{\Delta t} = -\frac{1}{2} \left\| \sqrt{\mu^{n+\frac{1}{2}}} \boldsymbol{E}(\boldsymbol{u}^{n+\frac{1}{2}}) \right\|^2 - \left\| \sqrt{M} \nabla G^{n+\frac{1}{2}} \right\|^2 - \left\| \frac{1}{\sqrt{\Gamma}} \frac{\phi^{n+1} - \phi^n}{\Delta t} \right\|_{\partial\Omega_w}^2 + \sum_{e \in \mathcal{T}(\partial\Omega_w)} B_e \tag{4.12}$$

where

$$\mathcal{F}_A^n = \int_\Omega \left[\frac{1}{2} \rho |\boldsymbol{u}^n|^2 + \lambda \left(\frac{1}{2} |\nabla \phi^n|^2 + f_0(\phi^n) \right) \right] d\boldsymbol{x} + \int_{\partial\Omega_w} f_w(\phi^n; \theta_A) ds \tag{4.13}$$

and

$$B_e = \begin{cases} 0 & \textit{if } 0 \geqslant L_A^* \geqslant L_R^* \\ \left(Df_w(\phi^n, \phi^{n+1}; \theta_A) - Df_w(\phi^n, \phi^{n+1}; \theta_R), \frac{\phi^{n+1} - \phi^n}{\Delta t} \right)_e & \textit{if } L_A^* \geqslant L_R^* > 0 \\ \left(\lambda \boldsymbol{n} \cdot \nabla \phi^{n+\frac{1}{2}} + Df_w(\phi^n, \phi^{n+1}; \theta_A), \frac{\phi^{n+1} - \phi^n}{\Delta t} \right)_e & \textit{otherwise} \end{cases}. \tag{4.14}$$

Proof. Taking $\hat{\boldsymbol{u}} = \boldsymbol{u}^{n+\frac{1}{2}}$, the left-hand side of (4.6) becomes

$$\begin{aligned} LHS &= \left(\rho \frac{\boldsymbol{u}^{n+1} - \boldsymbol{u}^n}{\Delta t}, \frac{\boldsymbol{u}^{n+1} + \boldsymbol{u}^n}{2} \right) \\ &\quad + \left(\bar{\boldsymbol{u}}^{n+\frac{1}{2}} \cdot \nabla \boldsymbol{u}^{n+\frac{1}{2}} + \frac{1}{2} (\nabla \cdot \bar{\boldsymbol{u}}^{n+\frac{1}{2}}) \boldsymbol{u}^{n+\frac{1}{2}}, \boldsymbol{u}^{n+\frac{1}{2}} \right) \\ &= \frac{\rho}{2\Delta t} \left(\|\boldsymbol{u}^{n+1}\|^2 - \|\boldsymbol{u}^n\|^2 \right) + \frac{1}{2} \left(\nabla \cdot \left(\bar{\boldsymbol{u}}^{n+\frac{1}{2}} \left| \boldsymbol{u}^{n+\frac{1}{2}} \right|^2 \right), 1 \right) \\ &= \frac{\rho}{2\Delta t} \left(\|\boldsymbol{u}^{n+1}\|^2 - \|\boldsymbol{u}^n\|^2 \right), \end{aligned} \tag{4.15}$$

where we have used the boundary condition $\bar{\boldsymbol{u}}^{n+\frac{1}{2}} \cdot \boldsymbol{n}|_{\partial\Omega} = \frac{3\boldsymbol{u}^{n+1} - \boldsymbol{u}^n}{2} \cdot \boldsymbol{n}\Big|_{\partial\Omega} = \boldsymbol{0}$ in the

last equality. It should be noted that this equation does not require $\nabla \cdot \boldsymbol{u}^n = 0$ to be exactly satisfied. The right-hand side of (4.6) becomes

$$\begin{aligned} RHS &= \left(p^{n+\frac{1}{2}}, \nabla \cdot \boldsymbol{u}^{n+\frac{1}{2}}\right) - \left(\mu^{n+\frac{1}{2}} \boldsymbol{E}(\boldsymbol{u}^{n+\frac{1}{2}}), \nabla \boldsymbol{u}^{n+\frac{1}{2}}\right) + \left(G^{n+\frac{1}{2}} \nabla \phi^{n+\frac{1}{2}}, \boldsymbol{u}^{n+\frac{1}{2}}\right) \\ &= \left(p^{n+\frac{1}{2}}, \nabla \cdot \boldsymbol{u}^{n+\frac{1}{2}}\right) - \|\sqrt{\mu^{n+\frac{1}{2}}} \boldsymbol{E}(\boldsymbol{u}^{n+\frac{1}{2}})\|^2 + \left(G^{n+\frac{1}{2}} \nabla \phi^{n+\frac{1}{2}}, \boldsymbol{u}^{n+\frac{1}{2}}\right). \end{aligned} \tag{4.16}$$

Since (4.7) is satisfied at each time level, it follows that $-\left(\nabla \cdot \left(\frac{\boldsymbol{u}^{n+1}+\boldsymbol{u}^n}{2}\right), \hat{p}\right) = 0$. By taking $\hat{p} = p^{n+\frac{1}{2}}$, we obtain

$$-\left(\nabla \cdot \boldsymbol{u}^{n+\frac{1}{2}}, p^{n+\frac{1}{2}}\right) = 0. \tag{4.17}$$

By taking $\hat{\phi} = G^{n+\frac{1}{2}}$, (4.8) leads to

$$\left(\frac{\phi^{n+1} - \phi^n}{\Delta t}, G^{n+\frac{1}{2}}\right) + \left(\boldsymbol{u}^{n+\frac{1}{2}} \cdot \nabla \phi^{n+\frac{1}{2}}, G^{n+\frac{1}{2}}\right) = -\left(M \nabla G^{n+\frac{1}{2}}, \nabla G^{n+\frac{1}{2}}\right). \tag{4.18}$$

We then take $\hat{G} = \frac{\phi^{n+1}-\phi^n}{\Delta t}$ in (4.9) and obtain

$$\begin{aligned} &\left(G^{n+\frac{1}{2}}, \frac{\phi^{n+1} - \phi^n}{\Delta t}\right) - \left(\frac{1}{\Gamma} \frac{\phi^{n+1} - \phi^n}{\Delta t}, \frac{\phi^{n+1} - \phi^n}{\Delta t}\right) \\ =& \left(\lambda \nabla \left(\frac{\phi^{n+1} + \phi^n}{2}\right), \nabla \left(\frac{\phi^{n+1} - \phi^n}{\Delta t}\right)\right) + \left(\lambda D f_0(\phi^n, \phi^{n+1}), \frac{\phi^{n+1} - \phi^n}{\Delta t}\right) \\ &+ \sum_{e \in \mathcal{T}(\partial \Omega_w)} \left(A^{n+\frac{1}{2}}, \frac{\phi^{n+1} - \phi^n}{\Delta t}\right)_e \\ =& \left(\frac{\lambda}{2}\left(|\nabla \phi^{n+1}|^2 - |\nabla \phi^n|^2\right), \frac{1}{\Delta t}\right) + \left(\lambda\left(f_0(\phi^{n+1}) - f_0(\phi^n)\right), \frac{1}{\Delta t}\right) \\ &+ \left(D f_w(\phi^n, \phi^{n+1}; \theta_A), \frac{\phi^{n+1} - \phi^n}{\Delta t}\right)_{\partial \Omega_w} \\ &+ \sum_{e \in \mathcal{T}(\partial \Omega_w)} \left(A^{n+\frac{1}{2}} - D f_w(\phi^n, \phi^{n+1}; \theta_A), \frac{\phi^{n+1} - \phi^n}{\Delta t}\right)_e \\ =& \frac{1}{\Delta t} \int_\Omega \left[\left(\frac{1}{2}\lambda |\nabla \phi^{n+1}|^2 + \lambda f_0(\phi^{n+1})\right) - \left(\frac{1}{2}\lambda |\nabla \phi^n|^2 + \lambda f_0(\phi^n)\right)\right] d\boldsymbol{x} \\ &+ \frac{1}{\Delta t} \int_{\partial \Omega_w} \left[f_w(\phi^{n+1}; \theta_A) - f_w(\phi^n; \theta_A)\right] ds - \sum_{e \in \mathcal{T}(\partial \Omega_w)} B_e. \end{aligned} \tag{4.19}$$

Finally, by summing up equations (4.15)–(4.18) and subtracting (4.19), we arrive at (4.12). □

Remark 2. *Since the proof is based on weak form and integration by parts, it can be easily extended to Galerkin methods with finite dimensional function spaces (Shen* et al. *2015). This energy law thus also applies to the fully discrete Galerkin finite element methods. The only additional requirement is that ϕ and G must share the same function space such that we can take $\hat{\phi} = G^{n+1/2}$ and $\hat{G} = \frac{\phi^{n+1}-\phi^n}{\Delta t}$.*

Remark 3. *The energy law* (4.12) *is dissipative except for the B_e term due to hystersis. We cannot prove this term to be non-positive from the weak from. However we can show $B_e \leqslant 0$ if the strong form* (3.3) *is satisfied.*

- *If* $0 > L_A^* > L_R^*$*, the contact line advances and we have the trivial relation* $B_e = 0$*.*
- *If* $L_A^* > L_R^* > 0$*, the contact line recedes according to the strong form* (3.3)*, and thus* $\phi^{n+1} - \phi^n \leqslant 0$*. Similar to the inequality* $f_w'(\phi, \theta_A) \geqslant f_w'(\phi; \theta_R)$*, it can be easily shown that* $Df_w(\phi^n, \phi^{n+1}; \theta_A) \geqslant Df_w(\phi^n, \phi^{n+1}; \theta_R)$ *for* $\phi^n, \phi^{n+1} \in [-1, 1]$*. Thus we have* $B_e \leqslant 0$ *when the contact line recedes. This corresponds to the dissipation term* $\mathcal{D}_{cah}$ *in Theorem 1.*
- *Otherwise, the contact line is pinned according to* (3.3)*. In this case* $\phi^{n+1} = \phi^n$ *and thus* $B_e = 0$*.*

It should be noted, however, that the weak form cannot exactly guarantee $\phi^{n+1} > \phi^n$ *when* $L_A^* > L_R^* > 0$ *or* $\phi^{n+1} = \phi^n$ *when* $L_A^* \geqslant 0 \geqslant L_R^*$*. Thus there might be regions with* $Be > 0$ *on wall boundaries in finite-element computations. But, in practice, we do expect the weak solution to be a reasonable approximation to the strong solution and thus* $B_e \leqslant 0$ *to be "approximately" satisfied.*

Remark 4. *In the absence of CAH, we have* $\theta_A = \theta_R$ *and thus* $B_e = 0$*. In this case,* (4.12) *recovers unconditional energy stability. It should be noted, however, that our numerical scheme is nonlinear and requires iterations. Thus the time step still cannot be too large in practical computations.*

Although we can not establish the energy stability for variable density problems, it does not raise severe stability concerns in practical computations as demonstrated later in Section 5.3.

4.2. *Numerical methods*

The equation system (4.6)–(4.9) are solved by the finite element method using the deal.ii library (Bangerth *et al.* 2007; Alzetta *et al.* 2018). Hierarchical adaptive meshes, quadrilateral in 2D and hexagonal in 3D, are used to discretize the computational domain. We use $Q2$ elements for $\boldsymbol{u}$, $Q1$ elements for p, and $Q3$ elements for ϕ and G. For easy implementation, we solve the flow equations (4.6) and (4.7) separately from the Cahn-Hilliard equations (4.8) and (4.9), and then couple them together using a Picard iteration.

The nonlinear system of (4.8) and (4.9) are solved by Newton's method. On each element face e on $\partial\Omega_w$, we compute two copies of chemical potential L_A and L_R, and their integrals L_A^* and L_R^* on e. The value of $A^{n+\frac{1}{2}}$ is then determined from (4.11). The linear system in each Newton step is solved by the generalized minimal residual method (GMRES) with the incomplete LU factorization (ILU) preconditioner.

The momentum equation (4.6) and the continuity equation (4.7) are solved by the mixed finite element method. Thanks to the explicit $\bar{\boldsymbol{u}}^{n+\frac{1}{2}}$, we have the following linear saddle point system:

$$\begin{bmatrix} A & B^T \\ B & 0 \end{bmatrix} \begin{bmatrix} U \\ P \end{bmatrix} = \begin{bmatrix} F \\ 0 \end{bmatrix}, \tag{4.20}$$

where U and P are solutions vectors for $\boldsymbol{u}^{n+1}$ and $p^{n+\frac{1}{2}}$, respectively. The asymmetric block A comes from the momentum equation except for the pressure term and the block B comes from the continuity equation. For 2D problems, where the number of degrees of freedom is typically below one million, we solve this system by the direct sparse linear solver UMFPACK (Davis 2004). For 3D problems, we adopt the grad-div stabilization and solve the saddle point system by GMRES with a block-triangular Schur complement preconditioner developed by Heister & Rapin (2013). Detailed implementation of this preconditioner can be found in Tutorial step-57 of deal.ii.

The solution procedure can be summarized as follows.

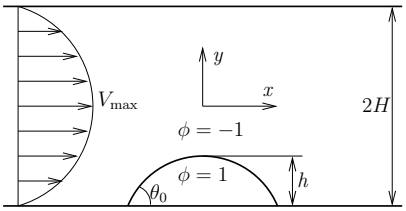

Figure 3: Schematic of a drop under shear in plane Poiseuille flow.

(i) Create an initial mesh which is refined at the interface and set the initial data $\boldsymbol{u}^0$ and ϕ^0.

(ii) For each time step $n \geqslant 0$, choose a proper Δt and perform the following steps until the stopping time is reached.

(a) Based on ϕ^n, locally refine or coarsen the mesh such that the mesh is the finest at the interface with $h_{min} \in [0.5\epsilon, \epsilon]$ and gets coarsened away from the interface. Transfer data from the old mesh to the new mesh if the mesh is modified.

(b) Let k denote the iteration step. Set $k = 0$ and $\boldsymbol{u}^{n+\frac{1}{2},0} = \bar{\boldsymbol{u}}^{n+\frac{1}{2}}$, and iterate over the following steps until convergence.

- Solve the Cahn-Hilliard equations (4.8) and (4.9) for $\phi^{n+1,k+1}$ and $G^{n+\frac{1}{2},k+1}$ based on ϕ^n and $\boldsymbol{u}^{n+\frac{1}{2},k}$.
- Solve the flow equations (4.6) and (4.7) for $\boldsymbol{u}^{n+1,k+1}$ and $p^{n+\frac{1}{2},k+1}$ based on $\boldsymbol{u}^n$, $\bar{\boldsymbol{u}}^{n+\frac{1}{2}}$, $\phi^{n+\frac{1}{2},k+1}$, and $G^{n+\frac{1}{2},k+1}$.
- $k = k + 1$.

(c) Update solution at t^{n+1}: $\boldsymbol{u}^{n+1} = \boldsymbol{u}^{n+1,k}$, $p^{n+\frac{1}{2}} = p^{n+\frac{1}{2},k}$, $\phi^{n+1} = \phi^{n+1,k}$, and $G^{n+\frac{1}{2}} = G^{nh,k}$.

In practice, we only need a few iterations in ii.b. For the computationally expensive 3D problems, we only compute two iterations, i.e., up to $k = 2$.

5. Results and discussions

5.1. *Drop deformation in plane Poiseuille flow*

We first validate our method by computing the drop deformation with pinned contact lines in plane Poiseuille flow (Schleizer & Bonnecaze 1999). This 2D test case has been widely used for validation purpose (e.g., Spelt 2005; Dupont & Legendre 2010; Huang *et al.* 2014; Liu *et al.* 2015). The computational domain is a $8H \times 2H$ rectangle with a drop adhered to the lower wall, as shown in Fig. 3(a). At the inlet, we impose a the fully developed flow velocity $u = \left[1 - \left(\frac{y}{H}\right)^2\right] V_{\max}$, where $V_{\max}$ is the maximum velocity along the centerline of the channel. At the outlet, we impose the zero traction condition. The lower and upper boundaries are stationary walls, where the velocity is set to zero. A drop is placed on the lower wall. Initially, the drop is a circular segment with contact angle $\theta_0 = 60°$. The drop has radius $R_0 = 0.9023H$ and height $h = 0.4511H$, such that its area is $0.5H^2$. Inertia is neglected and the viscosity ratio is unity, i.e., $\mu_1 = \mu_2 = \mu$. Following Schleizer & Bonnecaze (1999), we define the characteristic shear rate $E = \left.\frac{\partial u}{\partial y}\right|_{y=-H} = \frac{2V_{\max}}{H}$ and the capillary number $Ca = \frac{\mu E h}{\sigma} = \frac{\mu V_{\max}}{\sigma}\frac{2h}{H}$. To pin the contact line, we set $\theta_A = 170°$ and $\theta_R = 10°$.

For the Cahn-Hilliard equation, we introduce the following dimensionless parameters

(Yue *et al.* 2010; Yue & Feng 2011): the Cahn number

$$Cn = \frac{\epsilon}{H} \tag{5.1}$$

that characterizes the thickness of the interface,

$$S = \frac{l_D}{H} = \frac{\sqrt{M\mu}}{H} \tag{5.2}$$

that characterizes the slip due to Cahn-Hilliard diffusion, and

$$\Pi = \frac{1}{\mu \Gamma H} \tag{5.3}$$

that characterizes the wall energy relaxation rate. Here $l_D = \sqrt{M\mu}$ is the diffusion length in the phase-field method, which is the counterpart of slip length in the slip models. For this test case we choose $Cn = 0.01$, $S = 0.01$, and $\Pi = 0.1$. The computational mesh is adaptively refined at the interface and the mesh sizes are $h_{\min} = \frac{H}{128}$ at the interface and $h_{\max} = \frac{H}{8}$ in the bulk phases, as shown in Fig. 4(a). There are typically 5 layers of mesh cells in the diffuse interface (between $\phi = \pm 0.9$ contours), which guarantees the sufficient resolution of the interface (Yue *et al.* 2004, 2006). Thanks to the adaptive mesh refinement, there are only 3022 elements in the whole computational mesh corresponding to Fig. 4(a).

We take $\Delta t = 0.04 \frac{\mu H}{\sigma}$ and run the simulation for 1000 steps, which is sufficient for the flow to reach steady state. The numerical results are given in Fig. 4. For different capillary numbers, the $\phi = 0$ level sets match the boundary-integral curves very well. In theory, the contact lines should be pinned at $x/H = \pm 0.7814$. The contact line at the right is pinned very accurately for all Ca. In comparison, there is an observable error at the left contact line for $Ca = 0.15$: the intersection of $\phi = 0$ and the wall is shifted slightly downstream. This is because the contact angle is very small and the diffuse interface has a much larger intersection with the wall. This, in return, introduces more uncertainty to the exact location of the sharp interface.

5.2. *Advancing and receding interfaces in plane Poiseuille flow*

The contact lines in the previous section are pinned. In this subsection, we investigate the dynamics of moving contact lines. We consider the advancing and receding interfaces between two parallel plates, as shown in Fig. 5(a). The velocity and stress boundary conditions are the same as those in the previous subsection. The domain size is $10H \times 2H$. The interfaces are initially vertical lines located at $x = 3H$ and $6H$, respectively. For convenience, we refer to the contact line on the left as the receding contact line and the one on the right as the advancing contact line, although they may both get pinned.

We still neglect inertia and only consider matched viscosities. At steady state, the interfaces together with the contact lines move at the average velocity $\bar{V} = \frac{2}{3} V_{\max}$ of the Poiseuille flow. We thus define the capillary number as $Ca = \frac{\mu \bar{V}}{\sigma}$. In the following computations, we take $S = 0.01$, $\theta_A = 135°$, and $\theta_R = 75°$. Other parameters will be given in the detailed discussions.

The apparent contact angle is usually introduced to describe the macroscopic behavior of the interface and there is never a unified definition that works for all flow conditions. In this work, following Hoffman (1975), we compute a circular fit to the $\phi = 0$ level set, and then determine θ_{app} based on the intersection between the circular fit and the wall, as shown in Fig. 5(b). At small capillary numbers, the interface away from the contact line

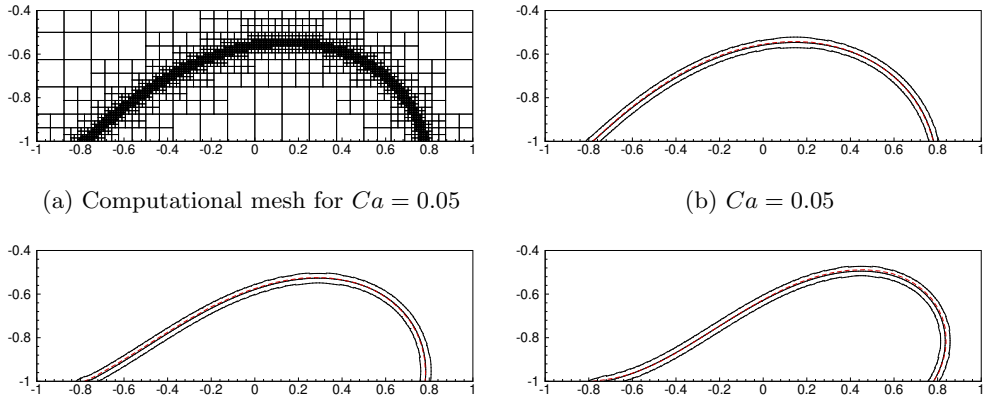

(a) Computational mesh for $Ca = 0.05$ (b) $Ca = 0.05$

(c) $Ca = 0.10$ (d) $Ca = 0.15$

Figure 4: An example of the computational mesh near the drop (a) and steady-state drop shapes (b–d). The (red) dashed curve denotes the interface obtained by Schleizer & Bonnecaze (1999) using a boundary integral method. The (black) solid curves denote the $\phi = -0.9, 0, 0.9$ contours by the phase-field method.

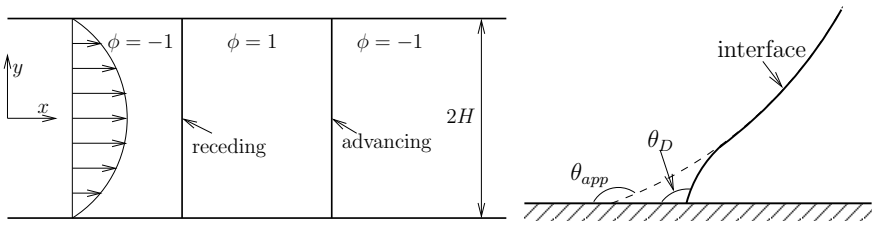

(a) (b)

Figure 5: Schematic of advancing and receding interfaces under plane Poiseuille flow (a) and a zoom at the contact line (b). The dashed line in (b) represents a circular fit to the deformed interface.

is very close to a circular arc, and θ_{app} defined above faithfully represents the interface behavior at the macroscopic length scale.

5.2.1. *Transient behavior of contact line*

We consider a small capillary number $Ca = 0.01$, under which the interfaces remain almost circular. For convenience, we define a dimensionless time $t^* = t\frac{\bar{V}}{H}$ and length $x^* = \frac{x}{H}$.

A typical interface evolution is given in Fig. 6. At $t^* = 0$, the vertical interfaces correspond to $\theta_D = 90° \in [\theta_R, \theta_A]$, and both contact lines are pinned. Under slow flow, each interface remains circular and $\theta_D = \theta_{app}$ when the contact line is pinned. We can thus easily find out the time instant to achieve a given θ_D by mass conservation and geometric relations:

$$t = \frac{1}{2}\frac{H}{\bar{V}}\left(\frac{\delta}{\sin^2\delta} - \cot\delta\right), \tag{5.4}$$

where $\delta = \left|\frac{\pi}{2} - \theta_D\right|$ is half of the central angle of the circular interface. Thus, theoretically, θ_D at the receding contact line achieves θ_R at $t^* = 0.0881$ and θ_D at the advancing

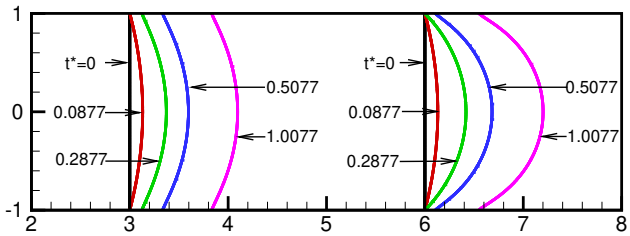

Figure 6: Snapshots of advancing and receding interfaces. $\Pi = 0.1$, $Ca = 0.01$. The dimensionless time step is set to $\Delta t^* = 10^{-4}$ initially and then gradually increases to 10^{-3}. Theoretically, the receding and advancing contact lines are depinned at $t^* = 0.0881$ and 0.2854, respectively, if the interfaces remain circular.

contact line achieves θ_A at $t^* = 0.2854$. These values agree very well with the numerical ones, which are approximately $t^* = 0.0877$ and $t^* = 0.2877$. After these time instants the contact lines start to move, which is also manifested by Fig. 7.

The value of Π affects the effective slip and thus the contact line dynamics once the contact line moves. The transient behaviors for $\Pi = 0.01$, 0.1, and 1 are given in Figs. 7 and 8. It should be noted that, for each contact line, the curves for different Π values collapse in the beginning. After the contact line is depinned, the effect of Π kicks in and the curves start to deviate from each other.

In Fig. 7, each contact line starts to accelerate after it is depinned and eventually achieves the steady-state contact line velocity, which equals $\bar{V}$ due to mass conservation. After normalization, this velocity corresponds to a slope of 1 in Fig. 7. The only exception is the advancing contact line with $\Pi = 1$, where a steady-state is never achieved and wetting failure occurs. Before reaching the steady state, the contact line velocity decreases as Π increases. This is easy to understand since the effective slip length decreases as Π increases (Yue & Feng 2011). In the context of phase-field method, this trend can also be explained from energy dissipation: the dissipation rate associated with the wall energy relaxation, $\int_{\partial\Omega_w} \Gamma \tilde{L}^2 ds = \int_{\partial\Omega_w} \frac{1}{\Gamma}\left(\frac{D\phi}{Dt}\right)^2 ds$, is proportional to $\Pi \propto \frac{1}{\Gamma}$ for the same amount of $\frac{D\phi}{Dt}$; this additional dissipation slows down the contact line motion.

The transient behaviors of contact angles are given in Fig. 8. The dynamic contact angle θ_D is measured based on the $\phi = 0$ level curve in the first two layers of cells adjacent to the wall. Compared to θ_{app} from circular fitting, θ_D is more prone to numerical errors, as manifested by the oscillations in the θ_D curves with $\Pi = 0.01$ in both Fig. 8(a) and (b). As Π increases, both θ_D and θ_{app} deviate more from the static contact angle, consistent with the analysis in Yue & Feng (2011). For the advancing contact line with $\Pi = 1$, we terminate the θ_{app} curve around $t^* = 0.6$ because the radius of the circular fit to the interface drops below H. In this case, θ_{app} exceeds 180° and is no longer physical, which usually signifies the onset of wetting failure.

5.2.2. *Steady-state contact line dynamics*

From matched asymptotic analysis, Cox (1986) showed that, to the leading order, the apparent contact angle $\theta_{\cancel{A}\,\mathrm{D}}$ follows

$$g(\theta_{\cancel{A}\,\mathrm{D}}) = g(\theta_S) + Ca \ln(\frac{W}{l_s}), \tag{5.5}$$

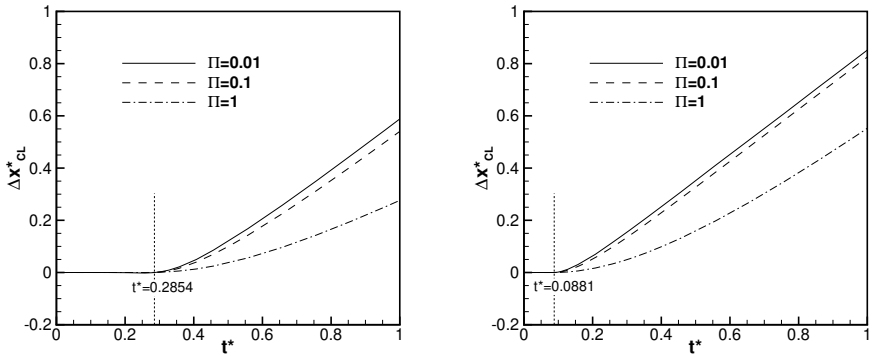

(a) Receding contact line. (b) Advancing contact line.

Figure 7: Displacements of contact lines. $Ca = 0.01$. Δx^*_{CL} is the normalized x-coordinate of the contact line relative to its initial position.

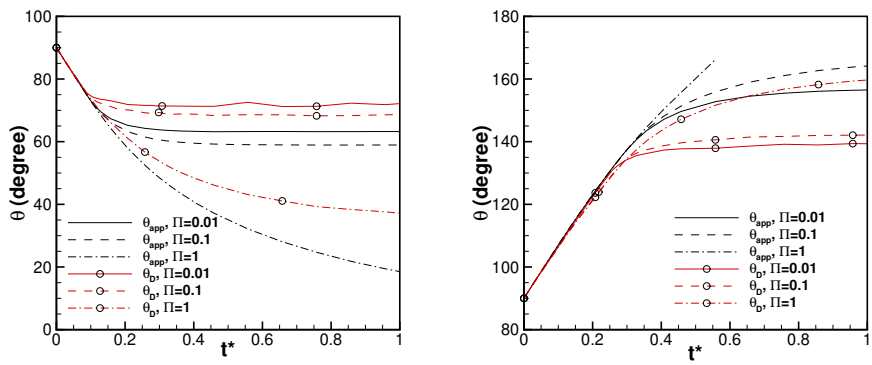

(a) Receding contact line. (b) Advancing contact line.

Figure 8: Transients of apparent and dynamic contact angles. $Ca = 0.01$.

where W is a characteristic macroscopic length, l_s is a slip length, and Ca is the capillary number defined based on the advancing fluid. The function g is given by

$$g(\theta) = \int_0^\theta \frac{ds}{f(s)},$$

where

$$f(\theta) = \frac{2\sin\theta\{\lambda_\mu^2(\theta^2-\sin^2\theta)+2\lambda_\mu[\theta(\pi-\theta)+\sin^2\theta]+[(\pi-\theta)^2-\sin^2\theta]\}}{\lambda_\mu(\theta^2-\sin^2\theta)[(\pi-\theta)+\sin\theta\cos\theta]+[(\pi-\theta)^2-\sin^2\theta](\theta-\sin\theta\cos\theta)}$$

and λ_μ is the viscosity ratio between the receding and advancing fluids. The steady-state apparent contact angle θ_{app} and the corresponding $g(\theta_{app})$ from phase-field simulations are given in Fig. 9, where the linear relation between $g(\theta_{app})$ and Ca is faithfully captured for both the advancing and receding contact lines at different Π values.

According to Yue *et al.* (2010), the slip length of the phase-field model due to interfacial mobility is approximately $2.5l_D$ for fluids with equal density. Furthermore, good agreements between Cox's formula and the phase-field method are achieved when W is taken to be the radius of the pipe for Poiseuille flows. For the plane Poiseuille flow

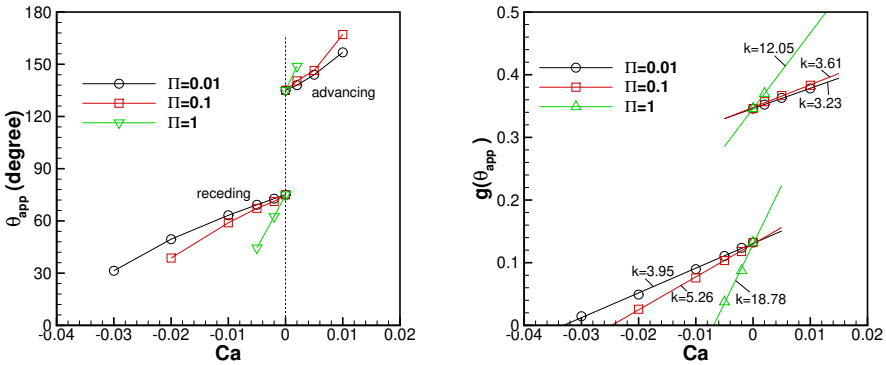

Figure 9: Steady-state dynamics of moving contact lines. $\theta_R = 75°$, $\theta_A = 135°$, $\lambda_\mu = 1$, $S = 0.01$, $Cn = 0.01$. The contact line advances if $Ca > 0$ and recedes if $Ca < 0$. The k values are the slopes of linear fits.

considered here, it is then reasonable to take W to be the half channel height H. When wall energy relaxation exists, the actual slip l_s differs from the $2.5l_D$. According to Yue & Feng (2011), we have

$$\frac{2\sqrt{2}}{3}\frac{\Pi}{Cn} = 5.63 \ln\left(\frac{2.5l_D}{\tilde{l}_s}\right) \tag{5.6}$$

for θ_D close to 90°. Thus the slope of the $g(\theta_{app}) \sim Ca$ curve should be

$$k = \ln\left(\frac{W}{l_s}\right) = \ln\left(\frac{H}{2.5l_D}\right) + \ln\left(\frac{2.5l_D}{\tilde{l}_s}\right) = \ln\left(\frac{1}{2.5S}\right) + \frac{2\sqrt{2}}{3}\frac{\Pi}{5.63Cn}.$$

This gives the theoretical slopes of $k = 3.86$, 5.36, and 20.44 for $\Pi = 0.01$, 0.1, and 1, respectively. These values agree reasonably well with the numerical values for the receding contact lines in Fig. 9(b). Much greater discrepancies are however observed on the advancing branch. This is probably because θ_D is too close to 180°. In this case, (5.6) is less accurate and we also expect larger errors in computing θ_{app}.

In summary, our current method captures the correct contact line dynamics, similar to the standard phase-field method without CAH (Yue *et al.* 2010; Yue & Feng 2011). The only complication is that θ_S may take different values, i.e., θ_R or θ_A, depending on whether the contact line recedes or advances.

5.2.3. *Pinning of contact line and choice of Γ*

As we have mentioned before, the discretized weak form can not guarantee the exact satisfaction of (3.3). That is, in real calculations, the contact line may still move even when it is supposed to be pinned. This actually happens when Π (or $\frac{1}{\Gamma}$) is not sufficiently large, as shown in Figs. 10 and 11(b). The advancing contact line with $\Pi = 0.001$ recedes slightly when it is supposed to be pinned at $t^* < 0.2854$. At $t^* = 0.2577$, the contact line with $\Pi = 0.1$ is nicely pinned at $x^* = 6$ while that with $\Pi = 0.001$ shifts upstream by about two grid cells. A close inspection of Fig.11(b) shows that the diffuse interface is slightly dilated near the wall. This type of pinning failure does not happen to the receding contact line, where the dynamic contact angle is very close to 90° before the contact line moves. Numerical tests with various contact angles and Π reveal that the

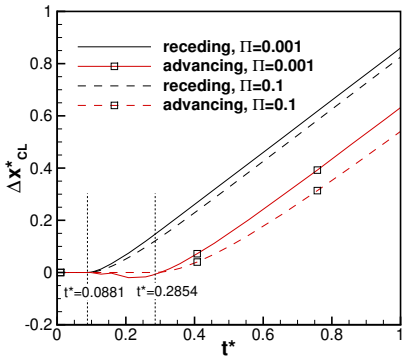

Figure 10: Pinning failure at a small Π. $\theta_R = 75°$, $\theta_A = 135°$, $Ca = 0.01$, $S = 0.01$, $Cn = 0.01$.

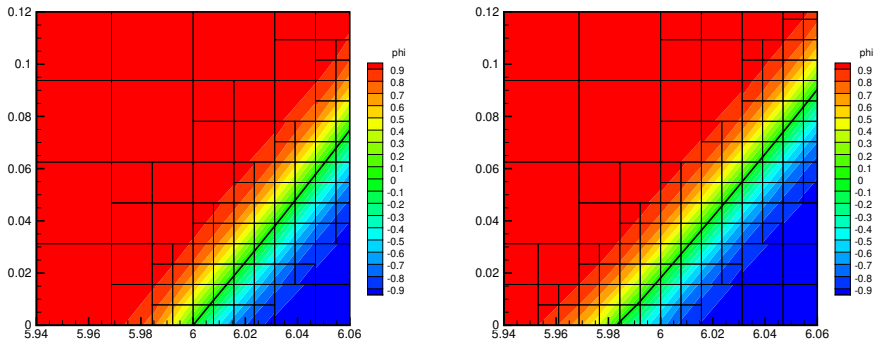

(a) $\Pi = 0.1$. (b) $\Pi = 0.001$.

Figure 11: ϕ contours at the vicinity of the advancing contact line at $t^* = 0.2577$. The contact line is supposed to be pinned at $x^* = 6$. The thick lines denote the interface ($\phi = 0$) and the thin lines are grid lines. $\theta_R = 75°$, $\theta_A = 135°$, $Ca = 0.01$, $S = 0.01$, $Cn = 0.01$.

pinning failure is more likely to occur for a smaller Π and when θ_D is further away from 90°.

To capture contact line pinning with good accuracy, we need a guideline for the choice of Π, i.e., Γ. By inspecting (4.12), we note that the energy dissipation rate on the solid wall $\partial\Omega_w$ for a pinned contact line can be written as

$$\mathcal{D}_w = \left(\frac{1}{\Gamma}\frac{\phi^{n+1}-\phi^n}{\Delta t}, \frac{\phi^{n+1}-\phi^n}{\Delta t}\right)_{\partial\Omega_w} - \left(\lambda \boldsymbol{n}\cdot\nabla\phi^{n+\frac{1}{2}} + Df_w(\phi^n,\phi^{n+1};\theta_A), \frac{\phi^{n+1}-\phi^n}{\Delta t}\right)_{\partial\Omega_w} \tag{5.7}$$

and is supposed to be zero since $\phi^{n+1} = \phi^n$. However, in practice, $\phi^{n+1} = \phi^n$ is not guaranteed by the weak form and we have no control over the sign of the second term of $\mathcal{D}_w$. A negative dissipation $\mathcal{D}_w < 0$ may thus occur and lead to numerical instability. A positive dissipation can be achieved if the first term overpowers the second term, which can be roughly satisfied by $\left|\frac{1}{\Gamma}\frac{\partial\phi}{\partial t}\right| \gtrsim |\lambda\boldsymbol{n}\cdot\nabla\phi|$. For a contact line moving with speed V

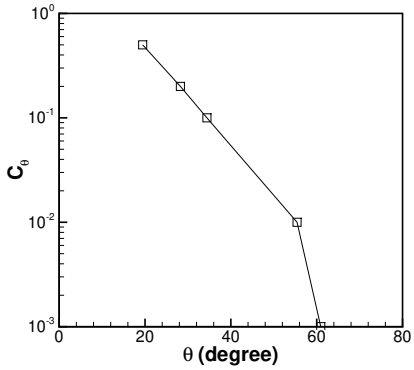

Figure 12: Numerical valus of C_θ. $\theta = \min(\theta_D, \pi - \theta_D)$.

and angle θ_D, we have $\left|\frac{\partial \phi}{\partial t}\right| \sim V|\nabla\phi||\sin\theta_D|$ and $|\lambda \boldsymbol{n} \cdot \nabla\phi| \sim \sigma\epsilon|\nabla\phi||\cos\theta_D|$. This leads to the approximate criterion

$$\Pi \gtrsim \frac{Cn}{Ca}\cot\theta_D \tag{5.8}$$

for numerical stability.

We have tested different combinations of Π, Ca, Cn, and S, with $\theta_R = 75°$ and $\theta_A = 135°$ being fixed. For the advancing contact line to falsely recede for the same displacement, Π has to be chosen such that it is proportional to Cn, inversely proportional to Ca, and independent of S, i.e., $\Pi \propto \frac{Cn}{Ca}$.

To investigate the influence of θ_D, we take $\theta_A = 170°$ so that pinning failure eventually occurs when θ_D is sufficiently close to 180°. We compute the advancing contact line with $\Pi = 0.001, 0.01, 0.1, 0.2$, and 0.5, until the contact line starts to move upstream for about one grid spacing $h_{\min}$. Other parameters are kept constant: $Ca = 0.01$, $S = 0.01$, and $Cn = 0.01$. The instantaneous θ_D is then recorded as the critical value that causes pinning failure. We have also tested $\Pi = 1$, but pinning failure never occurs. The numerical results, however, do not suggest a linear relation between the Π and $\cot\theta_D$. If we relax (5.8) to

$$\Pi \gtrsim \frac{Cn}{Ca}C_\theta, \tag{5.9}$$

then parameter C_θ can be numerically determined as shown in Fig. 12.

To achieve desired pinning performance in practical computations, we suggest using (5.9) together with Fig. 12 as a guideline for choosing Π. It should be noted that the derivations and numerical tests here are by no means rigorous.

5.2.4. *A computational strategy for hysteresis*

In the absence of CAH, a computational strategy has been proposed in Yue & Feng (2011) as follows. First, we choose a capillary width ϵ (or the dimensionless group Cn) based on the computational mesh that we can afford. Usually, we take $\epsilon \in [h_{\min}, 2h_{\min}]$, where $h_{\min}$ is the mesh size at the interface. This guarantees that the diffuse interface is sufficiently resolved. To reduce the influence of interfacial thickness on numerical results, Cn should be as small as possible, e.g., $Cn \leqslant 0.01$, which makes adaptive mesh refinement almost necessary. Second, we choose the mobility parameter M such that the diffusion length is well resolved: $l_D = \sqrt{M\mu} > \epsilon/4$ (or $S \geqslant Cn/4$ in the dimensionless form). This

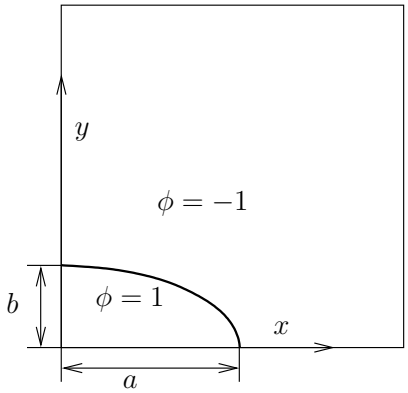

Figure 13: Schematic of an oscillating drop. The drop is initially elliptic with semi-axes $a = 2R_0$ and $b = 0.5R_0$, where R_0 is the effective drop radius.

guarantees that the numerical results are independent of ϵ and $h_{\min}$. Finally, we tune Γ (or the dimensionless group Π) to achieve the desired effective slip length.

This last step may however lead to a Π that is too small to numerically pin the contact line. Actually, the wall energy relaxation parameter Γ has no physical meaning when the contact line is pinned and we just need a non-zero number. Furthermore, there is no physical requirement that Γ must be a single-valued constant. We thus allow Γ to take different values depending on the status of the contact line and amend the third step above as follows. We estimate a Γ for pinning, denoted by Γ_P, based on (5.9) or numerical experiments. If Γ required for slip is greater Γ_P, then we impose Γ_P where the contact line is pinned and Γ elsewhere.

5.3. *Oscillating drop*

In this subsection, we consider an oscillating drop on a solid wall, where the contact line transitions between receding, pinning, and advancing. A schematic of the computational set up is given in Fig. 13. The initially elliptic drop will undergo oscillations due to inertia-capillary effects. The computational domain is a square of $4R_0 \times 4R_0$. Symmetry conditions are applied at the two vertical boundaries. Zero traction is applied on the upper boundary. The lower boundary is a solid wall with no-slip velocity and prescribed contact line conditions.

For convenience, we use effective drop radius R_0, drop density ρ_1, and surface tension σ to non-dimensionalize all the parameters, and denote the dimensionless parameters with a superscript *. For example, $t^* = t/t_c$ where $t_c = \sqrt{\frac{\rho R_0^3}{\sigma}}$ is the capillary time, viscosity $\mu^* = \frac{\mu}{\sqrt{\rho_1 \sigma R_0}}$, and energy $E^* = \frac{E}{\sigma R_0}$.

The fluid parameters are $\rho_1^* = 1$, $\rho_2^* = 0.01$, $\mu_1^* = 0.01$, $\mu_2^* = 0.001$, and $\sigma^* = 1$. This choice corresponds to a small Ohnesorge number

$$Oh = \frac{\mu_1}{\sqrt{\rho_1 \sigma R_0}} = 0.01, \tag{5.10}$$

such that the oscillation is not overdamped. For the diffuse interface, we choose $\epsilon^* = 0.01$, $M^* = 10^{-3}$, and $\Gamma^* = 10^3$. Some relevant dimensionless groups are $S = \frac{\sqrt{M\mu_1}}{R_0} = 3.16 \times 10^{-3}$ and $\Pi = \frac{1}{\mu_1 \Gamma R_0} = 0.1$. For the computational mesh, we choose $h^*_{\min} = \frac{1}{128}$ at the interface and $h^*_{\max} = \frac{1}{4}$ in the bulk.

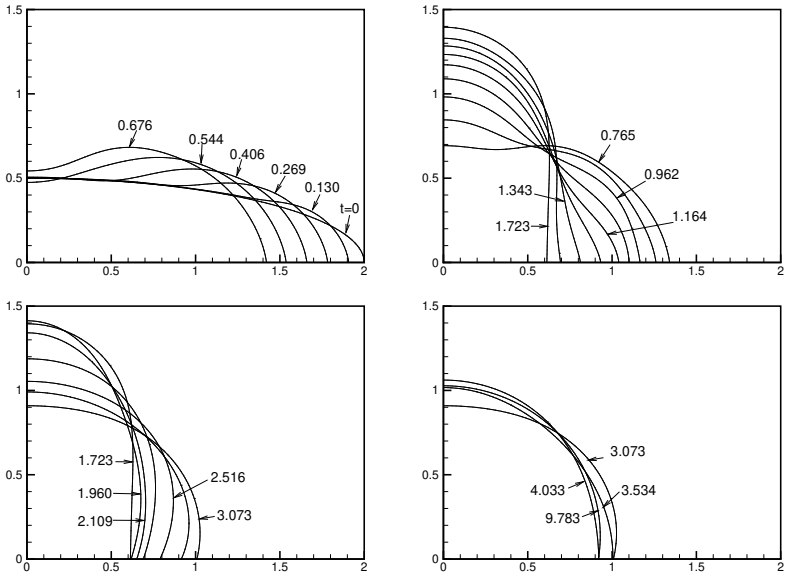

Figure 14: Snapshots of an oscillating drop with CAH. $\theta_R = 90°$, $\theta_A = 105°$. The contact line is pinned at $t^* \in [1.723, 1.960]$, $[3.073, 3.534]$, and $[4.033, \infty)$.

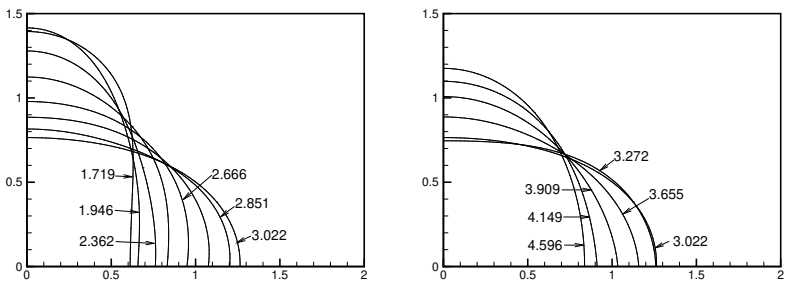

Figure 15: Snapshots of an oscillating drop without CAH. $\theta_R = \theta_A = 90°$.

We run three simulations with different contact angles: $(\theta_R, \theta_A) = (90°, 90°)$, $(90°, 105°)$, $(75°, 105°)$. The evolution of the drop interface for $(90°, 105°)$ and $(90°, 90°)$ are shown in Figs. 14 and 15, respectively. In the initial stage, the contact line moves to the left (i.e., recedes), and its dynamics is controlled by θ_R solely. Therefore these two cases are identical before the contact line stops at the leftmost position at $t^* \approx 1.723$. This is also manifested by the overlapping curves at $t^* \lesssim 1.723$ in Figs. 16 and 17. For $(\theta_R, \theta_A) = (90°, 105°)$, the contact line is pinned for a short period (around $t \in [1.723, 1.960]$) while the interface continues to protrude to the right. Once θ_D reaches $105°$ ($t \approx 1.960$), the contact line starts to move rightward. The contact line is pinned again around $t \in [3.073, 3.0534]$, and then retracts. Finally, the contact line stays pinned after $t^* = 4.033$ while the other part of the interface keeps oscillating. In contrast, there is no obvious contact line pinning for $(\theta_R, \theta_A) = (90°, 90°)$, i.e., when there is no CAH.

At $t^* \to \infty$, the drop will eventually settle to a static circular shape. The contact line position, i.e., the spreading radius, is related to the θ_{app} (which is also the same as θ_D)

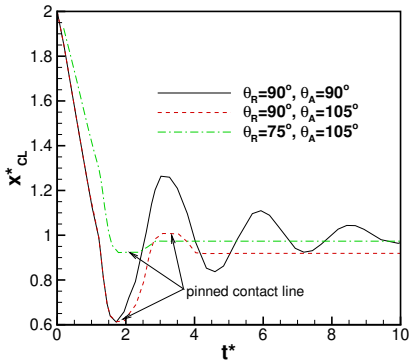

Figure 16: Contact line positions of oscillating drops. The plateaus denote the pinning of contact lines.

by

$$x^*_{CL} = \sqrt{\frac{\pi}{2[\theta_{app} - \frac{1}{2}\sin(2\theta_{app})]}}\sin\theta_{app}.$$

This gives $x^*_{CL} = 1.176$, 1, and 0.839 for $\theta_{app} = 75°$, 90°, and 105°, respectively. The trajectories of the contact line are given in Fig. 16. It is obvious that the contact line keeps oscillating around $x^*_{CL} = 1$ when there is no CAH. When there exists CAH, the contact line is finally pinned at $x^*_{CL} = 0.919$ and 0.973 for $(\theta_R, \theta_A) = (90°, 105°)$ and $(75°, 105°)$, both in the range determined by θ_R and θ_A. But the exact location of the final x^*_{CL} is also dependent on the transient process, i.e., the history of the contact line.

The evolution of free energies are given in Fig. 17. Here, the dimensionless free energies are computed as follows: kinetic energy $E^*_k = \frac{\int_\Omega \frac{1}{2}\rho|\boldsymbol{u}|^2 d\boldsymbol{x}}{\sigma R_0}$, mixing energy $E^*_m = \frac{\int_\Omega f_m d\boldsymbol{x}}{\sigma R_0}$, and wall energy $E^*_w = \frac{\int_{\partial\Omega_w} f_w(\phi;\theta_A) ds}{\sigma R_0}$. At $t^* = 0$, the whole system is static, which corresponds to a zero kinetic energy E^*_k and a maximum mixing energy E^*_m. As the drop retracts, part of the mixing energy is converted into kinetic energy. The repeated conversions between mixing and kinetic energies are manifested by the oscillatory curves in Fig. 17 (a) and (b). As time approaches $t^* = 10$, E^*_k drops to zero while E^*_m stabilizes around 1.57. The latter is consistent with the surface energy of a drop with $\theta_{app} = 90°$: $\frac{\pi}{2}\sigma R_0^2 = 1.571\sigma R_0^2$. The two curves with CAH stabilizes much faster than the one without due to additional dissipation from CAH.

In the initial retraction stage ($t^* \lesssim 1.723$), the E^*_k curve for $\theta_R = 75°$ deviates from the other two because contact line dynamics is determined by θ_R. Similarly, the sum $E^*_k + E^*_m$ decreases faster for $\theta_R = 75°$ in the initial retraction stage, as shown in Fig. 17(c). The evolution of the total free energy is provided in Fig. 17(d) to demonstrate the energy dissipative nature of our model. Although we can only prove the discrete energy law (4.12) for matched density and zero CAH, the numerical solutions satisfy a dissipative discrete energy law for a broader choice of parameters.

We also investigate the influence of the diffusive flux $\boldsymbol{J}$ on the phase-field simulations of interfacial flows with non-matched densities. We set $\boldsymbol{J} = 0$, i.e., neglecting the diffusive flux as in many previous phase-field simulations (e.g., Jacqmin 1999; Yue *et al.* 2006; Villanueva & Amberg 2006; Khatavkar *et al.* 2007*a*), and show the result for $\theta_R = \theta_A = 90°$ in Fig 17(d). The curve with $\boldsymbol{J} = 0$ is almost identical to the one considering diffusive flux. This is not surprising because the diffusive flux only occurs in the diffuse

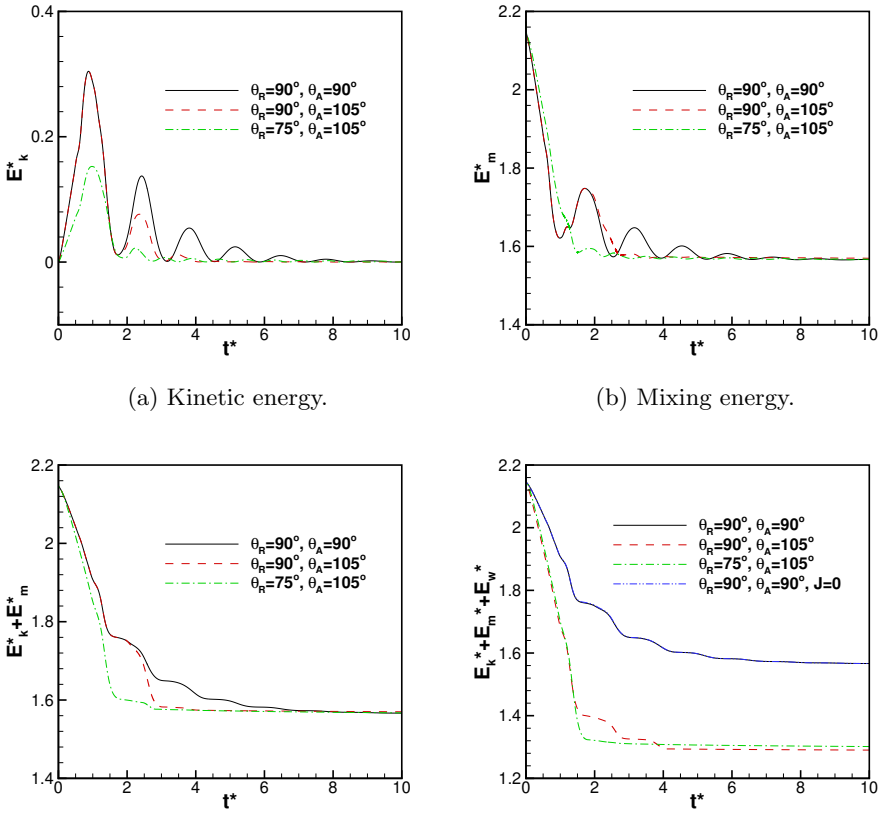

(a) Kinetic energy.

(b) Mixing energy.

(c) Total energy excluding wall energy.

(d) Total energy.

Figure 17: Time history of dimensionless free energies of oscillating drops.

interface region and its effect diminishes as Cn decreases. Thus in interfacial flows with non-matched densities, we expect the diffusive flux $\boldsymbol{J}$ to be negligible, at least in the case of $Cn \ll 1$.

5.4. *3D Drop on an inclined wall*

Our code can be easily switched to 3D, thanks to the dimension-independent programming advocated in deal.ii (Bangerth 2000). However, the discrete system resulted from the mixed finite element method is very costly to solve and thus we can only perform some preliminary 3D simulations. A more efficient projection-based flow solver is currently under development. The purpose of this subsection is only to demonstrate the capability of our hysteresis model in 3D flows.

We consider a drop on an inclined wall, as shown in Figs. 18 and 19. Similar to Section 5.3, we use drop density ρ_1, surface tension σ, and drop radius R_0 to non-dimensionalize all parameters. Due to symmetry in z-direction, we only compute half of the drop. The computational domain is a rectangular box defined by $[0, 8] \times [0, 3] \times [0, 3]$ with a hemispherical drop initially centered at $(5, 0, 0)$. The following dimensionless parameters are adopted: $\rho_1^* = 1$, $\rho_2^* = 0.01$, $\mu_1^* = 1$, $\mu_2^* = 0.01$, $\sigma^* = 1$, $R_0^* = 1$, $\epsilon^* = 0.02$, $M^* = 10^{-4}$, $\theta_R = 60°$, $\theta_A = 120°$, $\Gamma^* = 100$, and slope inclination angle $\alpha = 60°$. These

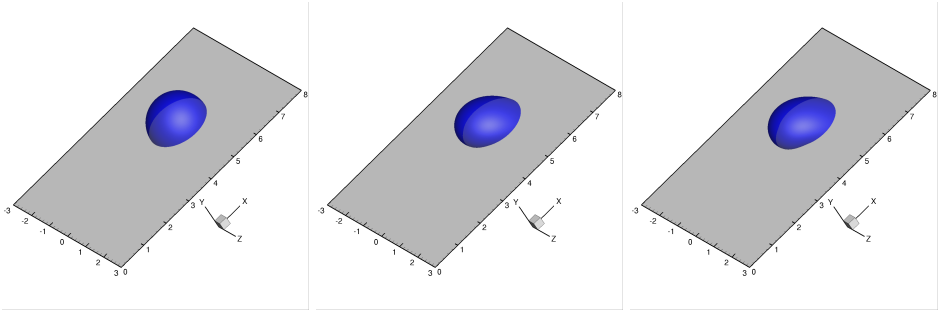

(a) $t^* = 0$ (b) $t^* = 4.52$ (c) $t^* = 24.52$

Figure 18: 3D drop sticking to an inclined wall. $Bo = 0.99$.

parameters correspond to the following dimensionless groups: $Cn = \frac{\epsilon}{R_0} = \epsilon^* = 0.02$, $S = \frac{\sqrt{M\mu_1}}{R_0} = \sqrt{M^*} = 10^{-2}$, $\Pi = \frac{1}{\mu_1 \Gamma R_0} = \frac{1}{\Gamma^*} = 0.01$, and $Oh = \frac{\mu_1}{\sqrt{\rho_1 \sigma R_0}} = 1$. We test $g^* = 1$ and $g^* = 2$, which correspond to the Bond numbers $Bo = \frac{(\rho_1 - \rho_2) g R_0^2}{\sigma} = (1 - \rho_2^*) g^* = 0.99$ and 1.98, respectively. For the computational mesh, we choose $h^*_{\min} = \frac{1}{64}$ at the interface and $h^*_{\max} = \frac{1}{8}$ in the bulk. The time step is set to $\Delta t^* = 0.01$ initially and is gradually increased to $\Delta t^* = 0.05$.

To achieve a good pinning performance, we take a smaller wall energy relaxation parameter $\Gamma_P^* = 10$ (such that $\Pi_P = 0.1$) when the contact line is pinned. It should be noted that this problem does not have a well-defined capillary number when the drop is pinned as shown in Fig. 18. In this case, we can do a rough estimation. Suppose we want the pinned contact line to move less than the grid spacing $h^*_{\min}$ during the whole simulation that lasts for $t^* \sim 20$. This gives $Ca \sim 10^{-3}$ and then (5.9) predicts $\Pi \gtrsim 0.02$ if we take $C_\theta = 0.001$ based on Fig. 12. Thus $\Pi_P = 0.1$ should be a safe choice.

It is well known that, due to CAH, relatively small drops have a tendency to stick to solid surfaces even when the latter is tilted. The critical parameters for the onset of drop sliding satisfy

$$(\rho_1 - \rho_2) g \sin\alpha = w\sigma(\cos\theta_R - \cos\theta_A), \tag{5.11}$$

where w is the width of the drop. This relation was first given by Furmidge (1962) based on experimental observations, and was later proved to be exact by Dussan V. & Chow (1983) as long as the footprint of the drop is convex. In practice, w is dependent on drop deformation and is unknown *a priori*. However, for an initially hemispherical drop, we can take the approximation $w \approx 2R_0$. This leads to the critical Bond number

$$Bo_c = \frac{\cos\theta_R - \cos\theta_A}{\frac{\pi}{3}\sin\alpha}, \tag{5.12}$$

which is 1.1027 for our chosen angles. It should be noted that Bo_c in the real situation may be more complicated and a problem-dependent prefactor needs to be included (Janardan & Panchagnula 2014).

Theoretically, the drop with $Bo = 0.99$ should stick to the slope while the drop with $Bo = 1.98$ should slide. This is confirmed by our numerical results in Figs. 18 and 19. The side views of the drops are given in Fig. 20, where the initial pinning of contact line is observed for both Bond numbers. It should be noted that the contact line in (a) moves slightly because of the initial transient and the fact that $Bo = 0.99$ is very close to the critical value. The top views of the drops, i.e., the contact lines, are given in Fig. 21. Theoretically, we expect a steadily sliding drop to have two straight sides parallel to

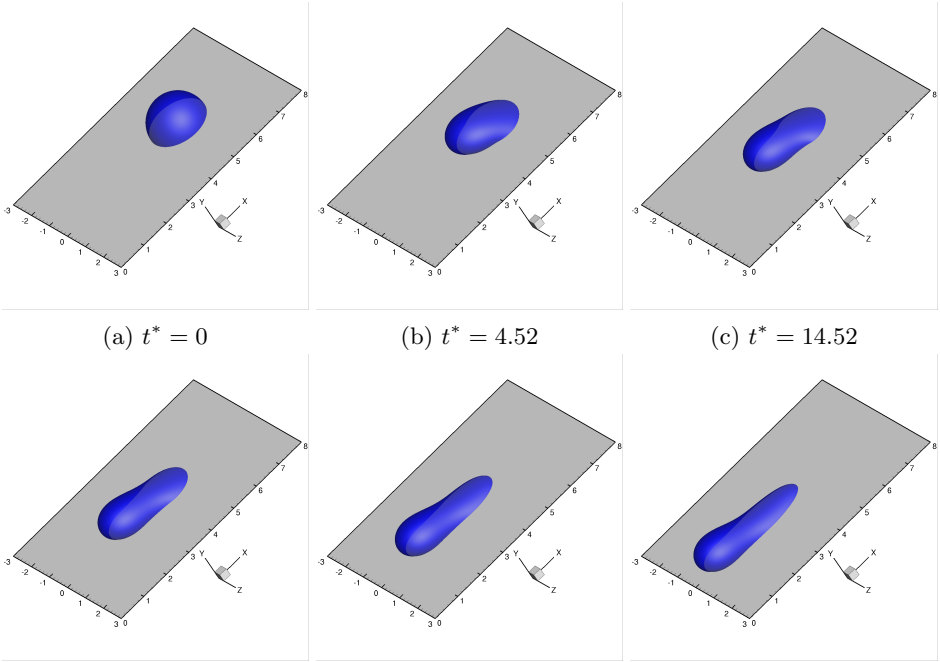

(a) $t^* = 0$ (b) $t^* = 4.52$ (c) $t^* = 14.52$

(d) $t^* = 24.52$ (e) $t^* = 34.52$ (f) $t^* = 44.52$

Figure 19: 3D drop sliding on an inclined wall. $Bo = 1.98$.

the moving direction (Furmidge 1962; Eral *et al.* 2013). This trend can be found from the contact line shape at $t^* = 44.52$. It should be noted that we have to terminate the simulation before a steady state was achieved because of the small computational domain. We will leave computations with realistic fluid properties and a larger computational domain for future work when a much more efficient flow solver is ready.

In the end, we investigate the dynamic contact angle θ_D. It is difficult to directly measure θ_D based on the level surface of $\phi = 0$ in 3D. We thus compute θ_D based on the relation $\cos\theta_D = \frac{\boldsymbol{n}\cdot\nabla\phi}{|\nabla\phi|}$ and the results are shown in Fig. 22. For the static drop in (a), $\theta_D \in [60°, 120°]$ along the whole contact line, consistent with the pinning condition. For the sliding drop in (b), $\theta_D > 120°$ at the leading edge, $\theta_D < 160°$ at the trailing edge, and $\theta_D \in [60°, 120°]$ along majority of the two sides. Correspondingly, the contact line advances at the leading edge, recedes at the trailing edge, and is pinned at the two sides as expected.

6. Concluding remarks

We have developed an energy-based boundary condition for CAH. The wall energy relaxation allows the two-phase system to deviate from equilibrium at the contact line. As a result, the microscopic dynamic contact angle θ_D, which is computed by the phase-field method, may differ from the prescribed static angle θ_S. The tendency of contact line motion can then be deduced from the difference between these two angles. When CAH exists, the single-valued θ_S is extended to a range of angles, namely, the hysteresis window $[\theta_R, \theta_A]$. Similarly, the tendency of contact line motion can be readily obtained from the computed θ_D and the prescribed θ_R and θ_A: the contact line advances if $\theta_D > \theta_A$, recedes if $\theta_D < \theta_R$, and is pinned otherwise. The major conclusions are summarized as follows.

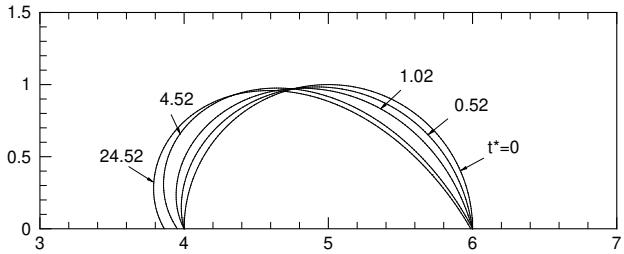

(a) $Bo = 0.99$

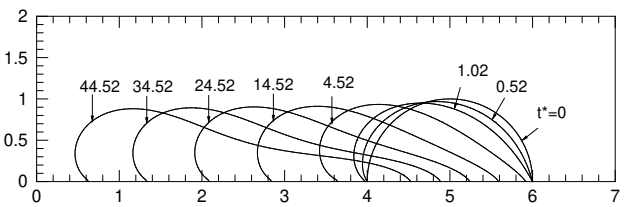

(b) $Bo = 1.98$

Figure 20: Side views of 3D drops on an inclined wall.

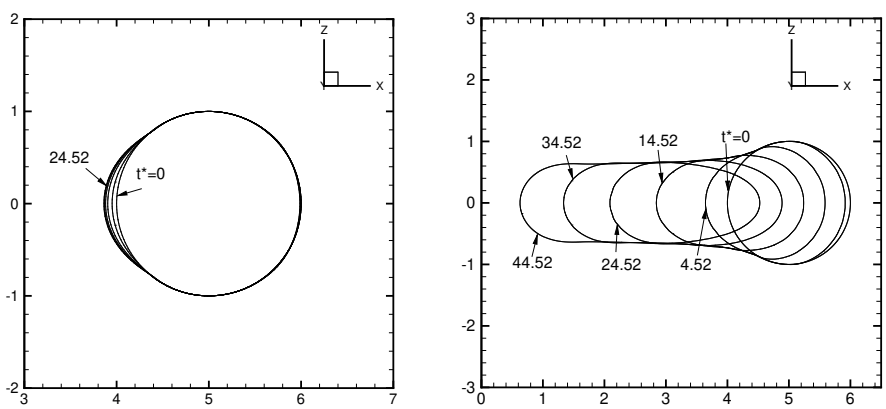

(a) $Bo = 0.99$ (b) $Bo = 1.98$

Figure 21: Evolution of contact lines.

(i) In the phase-field method, the relations between θ_D, θ_R and θ_A can be directly obtained from the values of the wall potentials defined based on θ_R and θ_A. As a result, our method captures CAH automatically, without the need to compute the contact line velocity or the dynamic contact angle.

(ii) When the contact line moves, our method automatically picks θ_R or θ_A depending on whether the contact line recedes or advances. The resulted contact line dynamics is exactly the same as the one without hysteresis. Furthermore, it agrees quantitatively with the well-established Cox theory.

(iii) The whole equation system satisfies a dissipative energy law and is thermody-

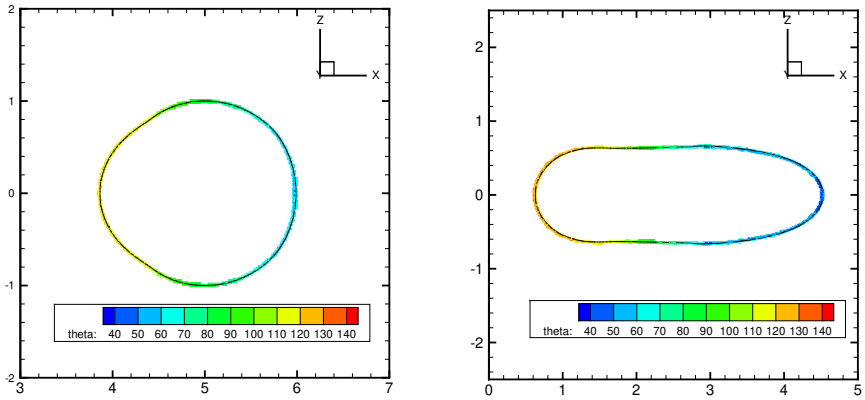

(a) $Bo = 0.99$, $t^* = 24.52$ (b) $Bo = 1.98$, $t^* = 44.52$

Figure 22: Dynamic contact angle.

namically consistent. In particular, the dissipation due to CAH is faithfully accounted for. Our Galerkin-type numerical discretization inherits this energy-dissipative property and is unconditionally energy-stable for matched density and zero hysteresis. Numerical tests show that the numerical scheme remains energy-dissipative for a broader range of parameters.

(iv) The wall energy relaxation parameter Γ is the only free parameter than can be tuned. We have provided a guideline for Γ to achieve good pinning performance when the contact line is pinned and to produce desired effective slip when the contact line is in motion.

(v) Our method has no limitation on dimensionality and it can be directly applied to three-dimensional flows.

The proposed method is easy to implement. If one has a phase-field code that allows wall energy relaxation, then hysteresis can be easily added with one additional copy of wall potential. Since wall potentials are only evaluated on the wall boundary, the additional computational cost is almost negligible.

A key component of our method is the dynamic contact angle θ_D that is computed and may deviate from θ_S. The same idea can be extended to Ren and E's version of GNBC (Ren & E 2007, 2011*a*), which also works for sharp-interface methods. We have developed a level-set method for CAH based on Ren and E's slip condition, and more details can be found in Zhang & Yue (2020).

Acknowledgement

This work was supported by the National Science Foundation (Grant DMS-1522604). The author thanks Prof. James J. Feng at the University of British Columbia for insightful comments on the draft of this manuscript. The author also acknowledges Advanced Research Computing at Virginia Tech for providing computational resources and technical support that have contributed to the results in this work.

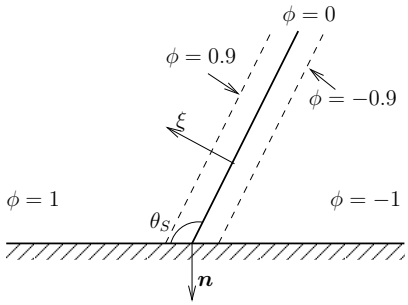

Figure A.1: Schematic of a contact line formed by a planar interface at static equilibrium. ξ is the local coordinate in the direction of $\nabla\phi$ with $\xi = 0$ at the center of the diffuse interface, and $\boldsymbol{n}$ is the unit normal to the solid wall. The contours of ϕ are parallel lines interesting the solid wall with θ_S.

Appendix A. Wall energy and contact angle

In this section, we provide a brief derivation of the wall energy formulation that is consistent with the ϕ profile across the diffuse interface. We consider a planar interface that intersects the wall with angle θ_S and assume the whole system to be in static equilibrium, as shown in Fig. A.1.

The equilibrium of the diffuse interface with mixing energy (2.2) requires

$$G = \lambda\left(-\frac{d^2\phi}{d\xi^2} + f_0'(\phi)\right) = 0, \tag{A 1}$$

where we have considered the fact that ϕ is only dependent on ξ for the planar interface (Yue *et al.* 2004). Multiplying this equation by $\frac{d\phi}{d\xi}$ gives

$$\frac{1}{2}\frac{d}{d\xi}\left(\frac{d\phi}{d\xi}\right)^2 = \frac{df_0}{d\xi}. \tag{A 2}$$

Since $f_0 = 0$ and $\frac{d\phi}{d\xi} = 0$ at $\xi = \pm\infty$, this equation can be integrated to give

$$\frac{d\phi}{d\xi} = \sqrt{2f_0} = \frac{1-\phi^2}{\sqrt{2}\epsilon}. \tag{A 3}$$

It should be noted that the hyperbolic tangent profile $\phi(\xi) = \tanh\left(\frac{\xi}{\sqrt{2}\epsilon}\right)$ can be obtained by further integrating (A 3) and taking $\phi(\pm\infty) = \pm 1$.

When the planar interface intersects the wall with angle θ_S, we get

$$\lambda\boldsymbol{n}\cdot\nabla\phi = \lambda(\boldsymbol{n}\cdot\boldsymbol{e}_\xi)\frac{d\phi}{d\xi} = \lambda\cos\theta_S\frac{1-\phi^2}{\sqrt{2}\epsilon} = \frac{3}{4}\sigma\cos\theta_S(1-\phi^2), \tag{A 4}$$

where $\boldsymbol{e}_\xi = \frac{\nabla\phi}{|\nabla\phi|}$ is the unit vector in the direction of ξ and we have used $\sigma = \frac{2\sqrt{2}}{3}\frac{\lambda}{\epsilon}$. Meanwhile, the equilibrium at the contact line requires

$$L(\phi, \nabla\phi; \theta_S) = \lambda\boldsymbol{n}\cdot\nabla\phi + f_w'(\phi) = 0, \tag{A 5}$$

from which we can obtain the wall energy

$$f_w(\phi) = -\int\frac{3}{4}\sigma\cos\theta_S(1-\phi^2)d\phi = -\sigma\frac{\phi(3-\phi^2)}{4}\cos\theta_S + c, \tag{A 6}$$

where c is an integration constant. Theoretically, c is determined by the interfacial

tensions between the fluids and the solid wall. However, the exact value of c does not matter in practice, since we only care about the variation in free energy rather than its absolute value. We simply take $c = 0$ in our simulations.

When a planar interface intersects the wall with a dynamic angle θ_D, similar to (A 4), we obtain

$$\lambda \boldsymbol{n} \cdot \nabla \phi = \lambda \cos \theta_D \frac{1 - \phi^2}{\sqrt{2}\epsilon} = -f_w'(\phi; \theta_D), \tag{A 7}$$

which is used in Section 3 to determine the relation between θ_D and the static contact angles θ_A and θ_R. Here the definition of $f_w(\phi; \theta)$ is given in (3.1). It should be noted that other forms of wall energy that do not satisfy (A 6), e.g., those in Qian *et al.* (2006*b*); Gao & Wang (2014); Luo *et al.* (2017), may lead to distortions of ϕ contours at the contact line and cannot guarantee (A 7).

Appendix B. Constitutive relations in phase-field model

In this section, motivated by the work of Ren & E (2011*b*) and the review article of Gomez & van der Zee (2017), we derive the constitutive relations in moving contact line problems based on thermodynamic principles. The same technique was also used in de Gennes & Prost (1993) to pose constitutive laws for nematic liquid crystals. Different from the work in Ren & E (2011*b*), we consider a general fluid domain without requiring $\boldsymbol{n} \cdot \boldsymbol{u} = 0$ on the boundary.

For an incompressible two-phase system in contact with a solid wall, the total free energy can be written as

$$\mathcal{F} = \int_{\Omega} \left(f_m(\phi, \nabla \phi) + \frac{1}{2} \rho |\boldsymbol{u}|^2 \right) d\boldsymbol{x} + \int_{\partial \Omega_w} f_w(\phi) ds, \tag{B 1}$$

where f_m is the mixing energy per unit volume, f_w is the surface energy per unit area on the wall, Ω is the domain occupied by the two-phase system, and $\partial \Omega_w \subset \partial \Omega$ denotes the solid wall surface which can only perform rigid-body motion. Here we have neglected external forces such as gravity, which can be easily accounted for. Ω is advected by fluid velocity $\boldsymbol{u}$ and $\partial \Omega_w$ by wall velocity $\boldsymbol{u}_w$. For an impermeable wall, $\boldsymbol{n} \cdot (\boldsymbol{u} - \boldsymbol{u}_w) = 0$ is satisfied, where $\boldsymbol{n}$ is the outward pointing unit normal to the boundary. We define slip velocity $\boldsymbol{u}_s = \boldsymbol{u} - \boldsymbol{u}_w$, and then impermeability yields $\boldsymbol{u}_s \cdot \boldsymbol{n} = 0$.

Different conventions have been used for tensor operations. In this work, we follow Soutas-Little (1999) and define the tensor operations as follows: $(\boldsymbol{A} \cdot \boldsymbol{B})_{ik} = A_{ij} B_{jk}$, $\boldsymbol{A} : \boldsymbol{B} = A_{ij} B_{ij}$, $(\boldsymbol{a} \cdot \boldsymbol{A})_j = a_i A_{ij}$, $(\boldsymbol{A} \cdot \boldsymbol{a})_i = A_{ij} a_j$, $(\boldsymbol{a} \otimes \boldsymbol{b})_{ij} = a_i b_j$, $(\nabla \boldsymbol{a})_{ij} = \frac{\partial}{\partial x_i} a_j$, and $(\nabla \cdot \boldsymbol{A})_j = \frac{\partial}{\partial x_i} A_{ij}$. Here $\boldsymbol{A}$ and $\boldsymbol{B}$ are second order tensors, $\boldsymbol{a}$ and $\boldsymbol{b}$ are vectors, and we have used the Einstein summation convention over repeated indices.

The flow needs to satisfy mass conservation

$$\frac{\partial \rho}{\partial t} + \nabla \cdot (\rho \boldsymbol{u}) = 0, \tag{B 2}$$

and the momentum equation

$$\rho \frac{D\boldsymbol{u}}{Dt} = \nabla \cdot \boldsymbol{T}, \tag{B 3}$$

were $\boldsymbol{T}$ is the stress term to be determined later and $\frac{D}{Dt} = \frac{\partial}{\partial t} + \boldsymbol{u} \cdot \nabla$ denotes the material derivative. To conserve mass of each phase, we adopt the following equation for ϕ:

$$\frac{D\phi}{Dt} = -\nabla \cdot \boldsymbol{j}, \tag{B 4}$$

where $\boldsymbol{j}$ is a diffusive flux to be determined. For simplicity, we assume zero diffusive flux on the whole boundary $\partial\Omega$: $\boldsymbol{n}\cdot\boldsymbol{j}=0$.

For the mixing energy, following the Reynolds transport theorem, we obtain

$$\begin{aligned}
&\frac{d}{dt}\int_\Omega f_m d\boldsymbol{x} = \int_\Omega \left(\frac{\partial f_m}{\partial t} + \nabla\cdot(\boldsymbol{u} f_m)\right) d\boldsymbol{x} \\
&= \int_\Omega \left[\frac{\partial f_m}{\partial \phi}\frac{\partial \phi}{\partial t} + \frac{\partial f_m}{\partial \nabla\phi}\cdot\frac{\partial \nabla\phi}{\partial t} + \boldsymbol{u}\cdot\left(\frac{\partial f_m}{\partial \phi}\nabla\phi + \frac{\partial f_m}{\partial \nabla\phi}\cdot(\nabla\nabla\phi)\right) + f_m\nabla\cdot\boldsymbol{u}\right] d\boldsymbol{x} \\
&= \int_\Omega \left[\left(\frac{\partial f_m}{\partial \phi} - \nabla\cdot\frac{\partial f_m}{\partial \nabla\phi}\right)\left(\frac{\partial \phi}{\partial t} + \boldsymbol{u}\cdot\nabla\phi\right) + \left(f_m\boldsymbol{I} - \frac{\partial f_m}{\partial \nabla\phi}\otimes\nabla\phi\right) : \nabla\boldsymbol{u}\right] d\boldsymbol{x} \\
&\quad + \oint_{\partial\Omega} \boldsymbol{n}\cdot\frac{\partial f_m}{\partial \nabla\phi}\left(\frac{\partial \phi}{\partial t} + \boldsymbol{u}\cdot\nabla\phi\right) ds.
\end{aligned} \tag{B 5}$$

Here we have recovered the chemical potential

$$G = \frac{\partial f_m}{\partial \phi} - \nabla\cdot\frac{\partial f_m}{\partial \nabla\phi} \tag{B 6}$$

and the stress term due to surface tension

$$\boldsymbol{\tau}_\phi = f_m\boldsymbol{I} - \frac{\partial f_m}{\partial \nabla\phi}\otimes\nabla\phi. \tag{B 7}$$

The surface tension term (B 7) can also be obtained by the virtual work principle without imposing the incompressibility condition. Considering the conserved phase dynamics (B 4), Eq. (B 5) can be further written as

$$\frac{d}{dt}\int_\Omega f_m d\boldsymbol{x} = \int_\Omega \left(\nabla G\cdot\boldsymbol{j} + \boldsymbol{\tau}_\phi : \nabla\boldsymbol{u}\right) d\boldsymbol{x} + \oint_{\partial\Omega}\left(\boldsymbol{n}\cdot\frac{\partial f_m}{\partial \nabla\phi}\right)\frac{D\phi}{Dt} ds, \tag{B 8}$$

where we have used the condition $\boldsymbol{n}\cdot\boldsymbol{j}=0$ on $\partial\Omega$.

For the kinetic energy, we get

$$\begin{aligned}
\frac{d}{dt}\int_\Omega \frac{1}{2}\rho|\boldsymbol{u}|^2 d\boldsymbol{x} &= \int_\Omega \left[\frac{\partial}{\partial t}\left(\rho\frac{|\boldsymbol{u}|^2}{2}\right) + \nabla\cdot\left(\boldsymbol{u}\rho\frac{|\boldsymbol{u}|^2}{2}\right)\right] d\boldsymbol{x} \\
&= \int_\Omega \left[\rho\frac{\partial \boldsymbol{u}}{\partial t}\cdot\boldsymbol{u} + \rho\boldsymbol{u}\cdot(\nabla\boldsymbol{u})\cdot\boldsymbol{u} + \frac{|\boldsymbol{u}|^2}{2}\left(\frac{\partial \rho}{\partial t} + \nabla\cdot(\rho\boldsymbol{u})\right)\right] d\boldsymbol{x} \\
&= \int_\Omega \rho\frac{D\boldsymbol{u}}{Dt}\cdot\boldsymbol{u} d\boldsymbol{x} = \int_\Omega (\nabla\cdot\boldsymbol{T})\cdot\boldsymbol{u} d\boldsymbol{x} = \oint_{\partial\Omega}\boldsymbol{n}\cdot\boldsymbol{T}\cdot\boldsymbol{u} ds - \int_\Omega \boldsymbol{T} : \nabla\boldsymbol{u} d\boldsymbol{x},
\end{aligned} \tag{B 9}$$

where we have used (B 2) in the third equality and (B 3) in the fourth equality.

Different from the mixing and kinetic energies, the wall energy is associated with the solid wall and is thus advected by $\boldsymbol{u}_w$ instead of $\boldsymbol{u}$. Since the wall surface is rigid (thus the surface divergence of $\boldsymbol{u}_w$ vanishes), we have

$$\begin{aligned}
\frac{d}{dt}\int_{\partial\Omega_w} f_w ds &= \int_{\partial\Omega_w}\left(\frac{\partial f_w}{\partial t} + \boldsymbol{u}_w\cdot\nabla f_w\right) ds \\
&= \int_{\partial\Omega_w}\left[f_w'(\phi)\frac{D\phi}{Dt} - f_w'(\phi)\boldsymbol{u}_s\cdot\nabla\phi\right] ds,
\end{aligned} \tag{B 10}$$

where we have used the relation $\boldsymbol{u}_s = \boldsymbol{u} - \boldsymbol{u}_w$.

Summing up (B 8), (B 9), and (B 10), we arrive at the energy equation

$$\begin{aligned}\frac{d}{dt}\mathcal{F} = &\int_{\Omega} [\nabla G \cdot \boldsymbol{j} - (\boldsymbol{T} - \boldsymbol{\tau}_\phi) : \nabla \boldsymbol{u}]\, d\boldsymbol{x} \\ &+ \int_{\partial\Omega_w} \left[\left(\boldsymbol{n} \cdot \frac{\partial f_m}{\partial \nabla\phi} + f_w'(\phi) \right) \frac{D\phi}{Dt} + (\boldsymbol{n} \cdot \boldsymbol{T} - f_w'(\phi)\nabla\phi) \cdot \boldsymbol{u}_s \right] ds \\ &+ \int_{\partial\Omega_w} \boldsymbol{n} \cdot T \cdot \boldsymbol{u}_w ds + \int_{\partial\Omega\backslash\partial\Omega_w} \boldsymbol{n} \cdot T \cdot \boldsymbol{u} ds + \int_{\partial\Omega\backslash\partial\Omega_w} \boldsymbol{n} \cdot \frac{\partial f_m}{\partial \nabla\phi} \frac{D\phi}{Dt} ds \end{aligned} \tag{B 11}$$

Here we have recovered the surface potential on the wall boundary $\partial\Omega_w$:

$$L(\phi, \nabla\phi) = \boldsymbol{n} \cdot \frac{\partial f_m}{\partial \nabla\phi} + f_w'(\phi). \tag{B 12}$$

The first two terms on the right hand side of (B 11) denote the dissipation rate in the system, which corresponds to entropy production due to irreversible processes. The third and the fourth terms account for the work done by the moving wall and other boundaries. The last term vanishes if we impose $\boldsymbol{n} \cdot \frac{\partial f_m}{\partial \nabla\phi} = 0$ on $\partial\Omega\backslash\partial\Omega_w$, i.e., the interface is perpendicular to the boundary. This corresponds to a neutral wetting condition, which is automatically satisfied if we use homogeneous natural boundary conditions for the Cahn-Hilliard equation on boundaries other than the wall.

The dissipation terms in (B 11) have been written in the form of products of the "generalized flux" and the corresponding "generalized force". According to the second law of thermodynamics, the irreversible processes must be entropy-productive, i.e., the associated energy dissipation rate must be non-negative. If we assume linear response, then energy dissipation is satisfied if we take

$$\boldsymbol{j} = -M\nabla G \quad \text{in } \Omega, \tag{B 13}$$

$$\boldsymbol{T} = -\mu(\nabla\boldsymbol{u} + (\nabla\boldsymbol{u})^T) + \boldsymbol{\tau}_\phi \quad \text{in } \Omega, \tag{B 14}$$

$$\frac{D\phi}{Dt} = -\Gamma L \quad \text{on } \partial\Omega_w, \tag{B 15}$$

$$-\beta\boldsymbol{u}_s = (\boldsymbol{n} \cdot \boldsymbol{T} - f_w'(\phi)\nabla\phi) \cdot (\boldsymbol{I} - \boldsymbol{n} \otimes \boldsymbol{n}) \quad \text{on } \partial\Omega_w, \tag{B 16}$$

with some positive parameters M, μ, Γ, and β. It should be noted that there might be other energy-dissipative constitutive relations than (B 13–B 16) and additional conditions are required to determine the physically correct constitutive relations. In (B 14), we have assumed that $\boldsymbol{T} - \boldsymbol{\tau}_\phi$ is a symmetric tensor, which is usually the case for physically relevant systems. In (B 16), we have used $\boldsymbol{u}_s = (\boldsymbol{I} - \boldsymbol{n} \otimes \boldsymbol{n}) \cdot \boldsymbol{u}_s$ which is a direct result of the impermeability condition $\boldsymbol{n} \cdot \boldsymbol{u}_s = 0$.

Plugging (B 13) into (B 4), we arrive at the Cahn-Hilliard equation

$$\frac{D\phi}{Dt} = \nabla \cdot (M\nabla G), \tag{B 17}$$

where M is called the mobility parameter.

For incompressible flows, $\boldsymbol{I} : \nabla\boldsymbol{u} = \nabla \cdot \boldsymbol{u} = 0$, thus an isotropic term $-p\boldsymbol{I}$ can be added to T without affecting dissipation. This parameter p, interpreted as pressure, serves as a Lagrange multiplier to enforce incompressibility. The momentum equation (B 3) thus reads

$$\rho\frac{D\boldsymbol{u}}{Dt} = \nabla \cdot \left[-p\boldsymbol{I} + \mu\left(\nabla\boldsymbol{u} + (\nabla\boldsymbol{u})^T\right) + \boldsymbol{\tau}_\phi \right]. \tag{B 18}$$

It should be noted that different forms of $\boldsymbol{\tau}_\phi$ have been used in the literature. For example, the isotropic term $f_m\boldsymbol{I}$ can be absorbed into $p\boldsymbol{I}$ such that one can effectively use $\tilde{\boldsymbol{\tau}}_\phi =$

$-\frac{\partial f_m}{\partial \nabla \phi} \otimes \nabla \phi$ to replace $\boldsymbol{\tau}_\phi$ (Yue *et al.* 2004). The forcing term due to $\boldsymbol{\tau}_\phi$ can also be written as

$$\begin{aligned}\nabla \cdot \boldsymbol{\tau}_\phi &= \nabla f_m - \nabla \cdot \left(\frac{\partial f_m}{\partial \nabla \phi} \otimes \nabla \phi \right) \\ &= \left(\frac{\partial f_m}{\partial \phi} \nabla \phi + \frac{\partial f_m}{\partial \nabla \phi} \cdot \nabla \nabla \phi \right) - \left[\left(\nabla \cdot \frac{\partial f_m}{\partial \nabla \phi} \right) \nabla \phi + \frac{\partial f_m}{\partial \nabla \phi} \cdot \nabla \nabla \phi \right] \\ &= G \nabla \phi, \end{aligned} \tag{B 19}$$

which is adopted in this work. Alternatively, a body force of the form $-\phi \nabla G = G \nabla \phi - \nabla (G\phi)$ was also found in the literature (Jacqmin 2000).

On the solid wall, the wall energy relaxation is governed by (B 15). Equation (B 16) is exactly the generalized Navier boundary condition (GNBC) (Qian *et al.* 2006*a*,*b*), which was originally derived based on Onsager's principle of minimum energy dissipation. It should be noted that the no-slip condition $\boldsymbol{u}_s = 0$, adopted by us and many others (Jacqmin 2000; Khatavkar *et al.* 2007*b*; Carlson *et al.* 2009), provides a simpler formulation which also satisfies energy dissipation.

Appendix C. Compressibility and Mass diffusion

For incompressible flows, we usually impose $\nabla \cdot \boldsymbol{u} = 0$. The mixture density ρ is governed by mass conservation (B 2). Meanwhile, given the densities of the pure phases, the mixture density can also be expressed as a function of the phase-field variable ϕ, and is therefore governed by the phase-field equation (B 17) unless $\rho'(\phi) = 0$. Thus the system in Appendix B may be over-determined if the two phases have different densities. To remedy this, the governing equations need to be modified and there are primarily two ways to derive physically consistent models.

The first method, proposed by Lowengrub & Truskinovsky (1998), is to consider the system as quasi-incompressible. In this treatment, ϕ is associated with mass fraction and the mixture velocity $\boldsymbol{u}$ is interpreted as the mass-averaged velocity. Then, from mass conservation (B 2), we can obtain

$$\nabla \cdot \boldsymbol{u} = -\frac{1}{\rho} \frac{D\rho}{Dt} = -\frac{\rho'(\phi)}{\rho} \frac{D\phi}{Dt}, \tag{C 1}$$

where $\frac{D\phi}{Dt}$ is determined by the Cahn-Hilliard equation. This equation replaces the original $\nabla \cdot \boldsymbol{u} = 0$. Moreover, due to compressibility, the mixing energy f_m has to be interpreted as a free energy per unit mass (and thus the total mixing energy is $\int_\Omega \rho f_m d\boldsymbol{x}$), which will cause substantial changes to the governing equations. Applications of this method can be found in Guo *et al.* (2014); Guo & Lin (2015).

The other method, first proposed by Ding *et al.* (2007) and later improved by Abels *et al.* (2012), associates ϕ with volume fraction and interprets $\boldsymbol{u}$ as the volume-averaged velocity. It can be easily shown that $\nabla \cdot \boldsymbol{u} = 0$ is still satisfied. However, this volume-averaged velocity modifies the mass conservation equation (B 2) to

$$\frac{\partial \rho}{\partial t} + \nabla \cdot (\rho \boldsymbol{u}) + \nabla \cdot \boldsymbol{J} = 0, \tag{C 2}$$

where $\boldsymbol{J}$ is the diffusive mass flux. It is obvious that

$$\boldsymbol{\nabla} \cdot J = -\frac{D\rho}{Dt} = -\rho'(\phi) \frac{D\phi}{Dt}. \tag{C 3}$$

Comparing this equation with (B 4) and considering the fact that $\rho'(\phi)$ is usually a

constant (see (2.16) for an example), we arrive at the identity

$$\boldsymbol{J} = \rho'(\phi)\boldsymbol{j}. \tag{C 4}$$

Considering (C 2) and the Galilean invariance requirement, the momentum equation (B 3) is updated to

$$\rho\frac{D\boldsymbol{u}}{dt} + \boldsymbol{J}\cdot\nabla\boldsymbol{u} = \nabla\cdot\tilde{\boldsymbol{T}}, \tag{C 5}$$

where $\tilde{\boldsymbol{T}} = \boldsymbol{T} + \boldsymbol{J}\otimes\boldsymbol{u}$ is an objective tensor that replaces the original $\boldsymbol{T}$ in (B 3). The readers are referred to Abels *et al.* (2012) for detailed derivations and Dong (2014, 2015) for extensions to N-phase systems with $N \geqslant 2$. It should be noted that the original formulation in Ding *et al.* (2007) is not Galilean invariant.

The method of Abels *et al.* allows us to use the existing numerical algorithms for incompressible flows with very little modification, and is thus more frequently seen in the recent literature (e.g., Shen & Yang 2015; Yu & Yang 2017). In the following, we only focus on this method.

With the modified mass conservation (C 2) and momentum equation (C 5), the time derivative of kinetic energy is updated to

$$\begin{aligned}
\frac{d}{dt}\int_\Omega \frac{1}{2}\rho|\boldsymbol{u}|^2 d\boldsymbol{x} &= \int_\Omega \left[\frac{|\boldsymbol{u}|^2}{2}\left(\frac{\partial\rho}{\partial t} + \nabla\cdot(\rho\boldsymbol{u})\right) + \rho\frac{D\boldsymbol{u}}{Dt}\cdot\boldsymbol{u}\right] d\boldsymbol{x} \\
&= \int_\Omega \left[-\frac{|\boldsymbol{u}|^2}{2}\nabla\cdot\boldsymbol{J} + (\nabla\cdot\tilde{\boldsymbol{T}} - \boldsymbol{J}\cdot\nabla\boldsymbol{u})\cdot\boldsymbol{u}\right] d\boldsymbol{x} \\
&= \oint_{\partial\Omega}\left(-\boldsymbol{n}\cdot\boldsymbol{J}\frac{|\boldsymbol{u}|^2}{2} + \boldsymbol{n}\cdot\tilde{\boldsymbol{T}}\cdot\boldsymbol{u}\right) ds - \int_\Omega \tilde{\boldsymbol{T}} : \nabla\boldsymbol{u} d\boldsymbol{x} \\
&= \oint_{\partial\Omega} \boldsymbol{n}\cdot\tilde{\boldsymbol{T}}\cdot\boldsymbol{u} ds - \int_\Omega \tilde{\boldsymbol{T}} : \nabla\boldsymbol{u} d\boldsymbol{x}
\end{aligned} \tag{C 6}$$

where we have used the zero-diffusive-flux condition $\boldsymbol{n}\cdot\boldsymbol{J} = \rho'(\phi)\boldsymbol{n}\cdot\boldsymbol{j} = 0$ on the boundary. This equation is identical to (B 9) expect for a different interpretation of the stress tensor. Consequently, all the equations remain the same as those in Appendix B, except for the modified mass conservation and momentum equations.

In our computations on oscillating drops (see Fig. 17d), however, we did not find any noticeable difference between the results from (B 3) and (C 5). Thus in practice, the effect of compressibility is only limited to the diffuse interface and has negligible effect on the macroscopic flow.

Declaration of Interests

The authors report no conflict of interest.

REFERENCES

Abels, H., Garcke, H. & Grün, G. 2012 Thermodynamically consistent, frame indifferent diffuse interface models for incompressible two-phase flows with different densities. *Math. Model. Methods Appl. Sci.* **22** (03), 1150013, arXiv: https://doi.org/10.1142/S0218202511500138.

Afkhami, S., Buongiorno, J., Guion, A., Popinet, S., Saade, Y., Scardovelli, R. & Zaleski, S. 2018 Transition in a numerical model of contact line dynamics and forced dewetting. *J. Comput. Phys.* **374**, 1061 – 1093.

Afkhami, S., Zaleski, S. & Bussmann, M. 2009 A mesh-dependent model for applying dynamic contact angles to vof simulations. *J. Comput. Phys.* **228**, 5370–5389.

Alzetta, G., Arndt, D., Bangerth, W., Boddu, V., Brands, B., Davydov, D., Gassmoeller, R., Heister, T., Heltai, L., Kormann, K., Kronbichler, M., Maier, M., Pelteret, J.-P., Turcksin, B. & Wells, D. 2018 The `deal.II` library, version 9.0. *J. Numer. Math.* **26** (4), 173–183.

Ba, Y., Liu, H., Sun, J. & Zheng, R. 2013 Color-gradient lattice boltzmann model for simulating droplet motion with contact-angle hysteresis. *Phys. Rev. E* **88**, 043306.

Bangerth, W. 2000 Using modern features of C++ for adaptive finite element methods: Dimension-independent programming in deal.II. In *Proceedings of the 16th IMACS World Congress 2000, Lausanne, Switzerland, 2000* (ed. Michel Deville & Robert Owens). Document Sessions/118-1.

Bangerth, W., Hartmann, R. & Kanschat, G. 2007 deal.II – a general purpose object oriented finite element library. *ACM Trans. Math. Softw.* **33** (4), 24/1–24/27.

Cahn, J. W. 1977 Critical-point wetting. *J. Chem. Phys.* **66**, 3667–3672.

Cahn, J. W. & Hilliard, J. E. 1958 Free energy of a nonuniform system. I. interfacial free energy. *J. Chem. Phys.* **28**, 258–267.

Carlson, A., Do-Quang, M. & Amberg, G. 2009 Modeling of dynamic wettting far from equilibrium. *Phys. Fluids* **21**, 121701.

Carlson, A., Do-Quang, M. & Amberg, G. 2011 Dissipation in rapid dynamic wetting. *J. Fluid Mech.* **682**, 213–240.

Cox, R. G. 1986 The dynamics of the spreading of liquids on a solid surface. Part 1. Viscous flow. *J. Fluid Mech.* **168**, 169–194.

Davis, T. A. 2004 Algorithm 832: Umfpack v4.3—an unsymmetric-pattern multifrontal method. *ACM Trans. Math. Softw.* **30** (2), 196–199.

Ding, H. & Spelt, P. D. M. 2008 Onset of motion of a three-dimensional droplet on a wall in shear flow at moderate reynolds numbers. *J. Fluid Mech.* **599**, 341–362.

Ding, H., Spelt, P. D. M. & Shu, C. 2007 Diffuse interface model for incompressible two-phase flows with large density ratios. *J. Comput. Phys.* **226** (2), 2078 – 2095.

Dong, S. 2014 An efficient algorithm for incompressible N-phase flows. *J. Comput. Phys.* **276**, 691 – 728.

Dong, S. 2015 Physical formulation and numerical algorithm for simulating n immiscible incompressible fluids involving general order parameters. *J. Comput. Phys.* **283**, 98 – 128.

Du, Q. & Nicolaides, R. 1991 Numerical analysis of a continuum model of phase transition. *SIAM J. on Numer. Analysis* **28** (5), 1310–1322, arXiv: https://doi.org/10.1137/0728069.

Dupont, J.-B. & Legendre, D. 2010 Numerical simulation of static and sliding drop with contact angle hysteresis. *J. Comput. Phys.* **229** (7), 2453 – 2478.

Dussan V., E. B. 1979 On the spreading of liquids on solid surfaces: static and dynamic contact lines. *Annu. Rev. Fluid Mech.* **11**, 371–400.

Dussan V., E. B. & Chow, R. T.-P. 1983 On the ability of drops or bubbles to stick to non-horizontal surfaces of solids. *J. Fluid Mech.* **137**, 1–29.

Eral, B., 't Mannetje, D. & Oh, J. 2013 Contact angle hysteresis: a review of fundamentals and applications. *Colloid polymer science* **291** (2), 247–260.

Extrand, C. W. 2002 Model for contact angles and hysteresis on rough and ultraphobic surfaces. *Langmuir* **18** (21), 7991–7999, arXiv: https://doi.org/10.1021/la025769z.

Extrand, C. W. 2016 Origins of wetting. *Langmuir* **32** (31), 7697–7706, pMID: 27459085, arXiv: https://doi.org/10.1021/acs.langmuir.6b01935.

Eyre, D. J. 1998 Unconditionally gradient stable time marching the Cahn-Hilliard equation. In *Computational and mathematical models of microstructural evolution (San Francisco, CA, 1998)*, *Mater. Res. Soc. Sympos. Proc.*, vol. 529, pp. 39–46. Warrendale, PA: MRS.

Fernández-Toledano, J.-C., Blake, T., Limat, L. & De Coninck, J. 2019 A molecular-dynamics study of sliding liquid nanodrops: Dynamic contact angles and the pearling transition. *J. Colloid Interface Sci.* **548**, 66 – 76.

Furmidge, C. 1962 Studies at phase interfaces. i. the sliding of liquid drops on solid surfaces and a theory for spray retention. *J. Colloid Sci.* **17** (4), 309 – 324.

Gao, L. & McCarthy, T. J. 2006 Contact angle hysteresis explained. *Langmuir* **22** (14), 6234–6237, pMID: 16800680, arXiv: https://doi.org/10.1021/la060254j.

Gao, M. & Wang, X.-P. 2014 An efficient scheme for a phase field model for the moving

contact line problem with variable density and viscosity. *J. Comput. Phys.* **272**, 704 – 718.

de Gennes, P. G. & Prost, J. 1993 *The Physics of Liquid Crystals*, 2nd edn. Oxford University Press.

Gomez, H. & van der Zee, K. G. 2017 Computational phase-field modeling. In *Encyclopedia of Computational Mechanics Second Edition*, pp. 1–35. American Cancer Society, arXiv: https://onlinelibrary.wiley.com/doi/pdf/10.1002/9781119176817.ecm2118.

Guermond, J.-L. & Quartapelle, L. 2000 A projection fem for variable density incompressible flows. *J. Comput. Phys.* **165** (1), 167 – 188.

Guo, Z. & Lin, P. 2015 A thermodynamically consistent phase-field model for two-phase flows with thermocapillary effects. *J. Fluid Mech.* **766**, 226–271.

Guo, Z., Lin, P. & Lowengrub, J. 2014 A numerical method for the quasi-incompressible Cahn-Hilliard-Navier-Stokes equations for variable density flows with a discrete energy law. *J. Comput. Phys.* **276**, 486 – 507.

Heister, T. & Rapin, G. 2013 Efficient augmented lagrangian-type preconditioning for the oseen problem using grad-div stabilization. *Int. J. for Numer. Methods Fluids* **71** (1), 118–134, arXiv: https://onlinelibrary.wiley.com/doi/pdf/10.1002/fld.3654.

Hoffman, R. L. 1975 A study of the advancing interface. *J. Colloid Interface Sci.* **50**, 228–241.

Huang, J.-J., Huang, H. & Wang, X. 2014 Numerical study of drop motion on a surface with stepwise wettability gradient and contact angle hysteresis. *Phys. Fluids* **26** (6), 062101, arXiv: https://doi.org/10.1063/1.4880656.

Iwamatsu, M. 2006 Contact angle hysteresis of cylindrical drops on chemically heterogeneous striped surfaces. *J. Colloid Interface Sci.* **297** (2), 772 – 777.

Jacqmin, D. 1999 Calculation of two-phase navier-stokes flows using phase-field modeling. *J. Comput. Phys.* **155** (1), 96 – 127.

Jacqmin, D. 2000 Contact-line dynamics of a diffuse fluid interface. *J. Fluid Mech.* **402**, 57–88.

Janardan, N. & Panchagnula, M. V. 2014 Effect of the initial conditions on the onset of motion in sessile drops on tilted plates. *Colloids Surfaces A: Physicochem. Eng. Aspects* **456**, 238 – 245.

Khatavkar, V. V., Anderson, P. D., Duineveld, P. C. & Meijer, H. E. H. 2007*a* Diffuse-interface modelling of droplet impact. *J. Fluid Mech.* **581**, 97–127.

Khatavkar, V. V., Anderson, P. D. & Meijer, H. E. H. 2007*b* Capillary spreading of a droplet in the partially wetting regime using a diffuse-interface model. *J. Fluid Mech.* **572**, 367–387.

Kusumaatmaja, H. & Yeomans, J. M. 2007 Modeling contact angle hysteresis on chemically patterned and superhydrophobic surfaces. *Langmuir* **23** (11), 6019–6032, pMID: 17451253, arXiv: https://doi.org/10.1021/la063218t.

Linder, N., Criscione, A., Roisman, I. V., Marschall, H. & Tropea, C. 2015 3D computation of an incipient motion of a sessile drop on a rigid surface with contact angle hysteresis. *Theor. Comput. Fluid Dyn.* **29** (5), 373–390.

Liu, H., Ju, Y., Wang, N., Xi, G. & Zhang, Y. 2015 Lattice boltzmann modeling of contact angle and its hysteresis in two-phase flow with large viscosity difference. *Phys. Rev. E* **92**, 033306.

Lowengrub, J. & Truskinovsky, L. 1998 Quasi-incompressible Cahn-Hilliard fluids and topological transitions. *Proc. Royal Soc. Lond. Ser. A: Math. Phys. Eng. Sci.* **454** (1978), 2617–2654, arXiv: https://royalsocietypublishing.org/doi/pdf/10.1098/rspa.1998.0273.

Luo, L., Wang, X.-P. & Cai, X.-C. 2017 An efficient finite element method for simulation of droplet spreading on a topologically rough surface. *J. Comput. Phys.* **349**, 233 – 252.

Maglio, M. & Legendre, D. 2014 Numerical simulation of sliding drops on an inclined solid surface. In *Computational and Experimental Fluid Mechanics with Applications to Physics, Engineering and the Environment* (ed. Leonardo Di G. Sigalotti, Jaime Klapp & Eloy Sira), pp. 47–69. Cham: Springer International Publishing.

Makkonen, L. 2017 A thermodynamic model of contact angle hysteresis. *The J. Chem. Phys.* **147** (6), 064703, arXiv: https://doi.org/10.1063/1.4996912.

Metzger, S. 2019 On stable, dissipation reducing splitting schemes for two-phase flow of electrolyte solutions. *Numer. Algorithms* **80** (4), 1361–1390.

Prabhala, B. & Panchagnula, M.V. anbd Vedantam, S. 2013 Three-dimensional equilibrium shapes of drops on hysteretic surfaces. *Colloid Polym. Sci.* **291**, 279–289.

Qian, T., Wang, X.-P. & Sheng, P. 2003 Molecular scale contact line hydrodynamics of immiscible flows. *Phys. Rev. E* **68**, 016306.

Qian, T., Wang, X.-P. & Sheng, P. 2006*a* Molecular hydrodynamics of the moving contact line in two-phase immiscible flows. *Commun. Comput. Phys.* **1**, 1–52.

Qian, T., Wang, X.-P. & Sheng, P. 2006*b* A variational approach to moving contact line hydrodynamics. *J. Fluid Mech.* **564**, 333–360.

Quéré, D. 2008 Wetting and roughness. *Annu. Rev. Mater. Res.* **38** (1), 71–99, arXiv: https://doi.org/10.1146/annurev.matsci.38.060407.132434.

Rahimi, P. & Ward, C. A. 2005 Contact angle hysteresis on smooth and homogenous surfaces in gravitational fields. *Microgravity - Sci. Technol.* **16** (1), 231–235.

Ren, W. & E, W. 2007 Boundary conditions for the moving contact line problem. *Phys. Fluids* **19**, 022101.

Ren, W. & E, W. 2011*a* Contact line dynamics on heterogeneous surfaces. *Phys. Fluids* **23**, 072103.

Ren, W. & E, W. 2011*b* Derivation of continuum models for the moving contact line problem based on thermodynamic principles. *Commun. Math. Sci.* **9**, 597–606.

Schleizer, A. D. & Bonnecaze, R. T. 1999 Displacement of a two-dimensional immiscible droplet adhering to a wall in shear and pressure-driven flows. *J. Fluid Mech.* **383**, 29–54.

Shen, J., Xu, J. & Yang, J. 2018 The scalar auxiliary variable (sav) approach for gradient flows. *J. Comput. Phys.* **353**, 407 – 416.

Shen, J. & Yang, X. 2010 Numerical approximations of Allen-Cahn and Cahn-Hilliard equations. *Discret. & Continuous Dyn. Syst. - A* **28**, 1669–1691.

Shen, J. & Yang, X. 2015 Decoupled, energy stable schemes for phase-field models of two-phase incompressible flows. *SIAM J. on Numer. Analysis* **53** (1), 279–296, arXiv: https://doi.org/10.1137/140971154.

Shen, J., Yang, X. & Yu, H. 2015 Efficient energy stable numerical schemes for a phase field moving contact line model. *J. Comput. Phys.* **284**, 617 – 630.

Shin, S., Chergui, J. & Juric, D. 2018 Direct simulation of multiphase flows with modeling of dynamic interface contact angle. *Theor. Comput. Fluid Dyn.* **32** (5), 655–687.

Soutas-Little, R. W. 1999 *Elasticity*. New York: Dover Publications.

Spelt, P. D. 2005 A level-set approach for simulations of flows with multiple moving contact lines with hysteresis. *J. Comput. Phys.* **207** (2), 389 – 404.

Vedantam, S. & Panchagnula, M. V. 2007 Phase field modeling of hysteresis in sessile drops. *Phys. Rev. Lett.* **99**, 176102.

Villanueva, W. & Amberg, G. 2006 Some generic capillary-driven flows. *Int. J. Multiph. Flow* **32** (9), 1072 – 1086.

Voinov, O. V. 1976 Hydrodynamics of wetting. *J. Fluid Mech.* **11** (5), 714–721, translated from Izvestiya Akademii Nauk SSSR, Mekhanika Zhidkosti i Gaza, No. 5, pp. 76–84, September–October, 1976.

Wang, L., Huang, H.-B. & Lu, X.-Y. 2013 Scheme for contact angle and its hysteresis in a multiphase lattice boltzmann method. *Phys. Rev. E* **87**, 013301.

Whyman, G., Bormashenko, E. & Stein, T. 2008 The rigorous derivation of Young, Cassie-Baxter and Wenzel equations and the analysis of the contact angle hysteresis phenomenon. *Chem. Phys. Lett.* **450** (4), 355 – 359.

Wu, S. & Ma, M. 2017 A contact angle hysteresis model based on the fractal structure of contact line. *J. Colloid Interface Sci.* **505**, 995 – 1000.

Wylock, C., Pradas, M., Haut, B., Colinet, P. & Kalliadasis, S. 2012 Disorder-induced hysteresis and nonlocality of contact line motion in chemically heterogeneous microchannels. *Phys. Fluids* **24** (3), 032108, arXiv: https://doi.org/10.1063/1.3696860.

Xu, X. & Wang, X. 2011 Analysis of wetting and contact angle hysteresis on chemically patterned surfaces. *SIAM J. on Appl. Math.* **71** (5), 1753–1779, arXiv: https://doi.org/10.1137/110829593.

Xu, X. & Wang, X. 2013 The modified Cassie's equation and contact angle hysteresis. *Colloid Polym. Sci.* **291** (2), 299–306.

Yang, X. 2016 Linear, first and second order and unconditionally energy stable numerical

schemes for the phase field model of homopolymer blends. *J. Comput. Phys.* **302**, 509–523.

Yu, H. & Yang, X. 2017 Numerical approximations for a phase-field moving contact line model with variable densities and viscosities. *J. Comput. Phys.* **334**, 665 – 686.

Yue, P. & Feng, J. J. 2011 Wall energy relaxation in the Cahn-Hilliard model for moving contact lines. *Phys. Fluids* **23**, 012106.

Yue, P., Feng, J. J., Liu, C. & Shen, J. 2004 A diffuse-interface method for simulating two-phase flows of complex fluids. *J. Fluid Mech.* **515**, 293–317.

Yue, P., Zhou, C. & Feng, J. J. 2010 Sharp-interface limit of the Cahn-Hilliard model for moving contact lines. *J. Fluid Mech.* **645**, 279–294.

Yue, P., Zhou, C., Feng, J. J., Ollivier-Gooch, C. F. & Hu, H. H. 2006 Phase-field simulations of interfacial dynamics in viscoelastic fluids using finite elements with adaptive meshing. *J. Comput. Phys.* **219**, 47–67.

Zhang, J. & Yue, P. 2020 A level-set method for moving contact lines with contact angle hysteresis. *J. Comput. Phys.* In revision.